Chemical Geology 550 (2020) 119649

Contents lists available at ScienceDirect

Chemical Geology

journal homepage: www.elsevier.com/locate/chemgeo

The geochemical and mineralogical fingerprint of West Antarctica's weak underbelly: Pine Island and Thwaites glaciers

Patric Simões Pereira[a,b,*], Tina van de Flierdt[b], Sidney R. Hemming[c], Thomas Frederichs[d], Samantha J. Hammond[e], Stefanie Brachfeld[f], Cathleen Doherty[g], Gerhard Kuhn[h], James A. Smith[i], Johann P. Klages[h], Claus-Dieter Hillenbrand[i]

[a] Grantham Institute for Climate Change and the Environment, Imperial College London, South Kensington Campus, London SW7 2AZ, UK
[b] Department of Earth Science and Engineering, Imperial College London, South Kensington Campus, London SW7 2AZ, UK
[c] Department of Earth and Environmental Sciences and Lamont-Doherty Earth Observatory of Columbia University, Palisades, NY 10964, USA
[d] Faculty of Geosciences, University of Bremen, Bremen 28359, Germany
[e] Department of Environment, Earth and Ecosystems, The Open University, Walton Hall, Milton Keynes MK7 6AA, UK
[f] Department of Earth and Environmental Studies, Montclair State University, Montclair, NJ 07043, USA
[g] Environmental and Occupational Health Sciences Institute, Rutgers University, Piscataway, NJ 08854, USA
[h] Alfred-Wegener-Institut, Helmholtz-Zentrum für Polar- und Meeresforschung, Marine Geosciences, Bremerhaven 27568, Germany
[i] British Antarctic Survey, High Cross, Madingley Road, Cambridge CB3 0ET, UK

ARTICLE INFO

Editor: Catherine Chauvel

Keywords:
West Antarctic Ice Sheet
Sediment provenance
Geochemistry
Pine Island Glacier
Thwaites Glacier

ABSTRACT

The marine-based West Antarctic Ice Sheet (WAIS) is considered the most unstable part of the Antarctic Ice Sheet, with particular vulnerability in the Amundsen Sea sector where glaciers are melting at an alarming rate. Far-field sea-level data and ice-sheet models have pointed towards at least one major WAIS disintegration during the Late Quaternary, but direct evidence for past collapse(s) from ice-proximal geological archives remains elusive. In order to facilitate geochemical and mineralogical tracing of the two most important glaciers draining into the Amundsen Sea, i.e. Pine Island Glacier (PIG) and Thwaites Glacier (TG), we here provide the first multi-proxy provenance analysis of 26 seafloor surface sediment samples from Pine Island Bay.

Our data show that the fingerprints of detritus delivered by PIG and TG are clearly distinct near the ice-shelf fronts of both ice-stream systems for all grain sizes and proxies investigated. Glacial detritus delivered by PIG is characterised by low ε_{Nd} values (~ -9), high $^{87}Sr/^{86}Sr$ ratios (~0.728), low smectite content (<10%), and hornblende and biotite grains with Late Permian to Jurassic (170–270 Ma) cooling ages. In contrast, glacigenic detritus delivered by TG is characterised by higher ε_{Nd} values (~ -4), lower $^{87}Sr/^{86}Sr$ ratios (0.714), higher smectite (20%) and kaolinite content (37%), biotite and hornblende grains with $^{40}Ar/^{39}Ar$ cooling ages of <40 Ma and ~115 Ma, and high content of mafic minerals.

The geochemical and mineralogical fingerprints for PIG and TG reported here provide novel insights into sub-ice geology and allow us to trace both drainage systems in the geological past, under environmental conditions more similar to those envisioned in the next 50 to 100 years.

1. Introduction

The West Antarctic Ice Sheet (WAIS) is considered capable of rapid partial or even total collapse, resulting in up to 4.3 m of global sea level rise (Fretwell et al., 2013), which may have occurred during Late Quaternary interglacials (e.g. Scherer et al., 1998) and may occur again in the future (DeConto and Pollard, 2016). Of particular interest are Pine Island Glacier (PIG) and Thwaites Glacier (TG), two ice streams draining approximately 32% of the WAIS into Pine Island Bay in the southeastern Amundsen Sea Embayment (Fig. 1). The combined drainage basins of the two glaciers are often referred to as the "weak underbelly" of the WAIS, i.e., the portion that is most susceptible to rapid collapse (e.g. Hughes, 1981), although its exact extent has recently been refined to comprise the TG drainage basin only (Holt et al., 2006; Vaughan et al., 2006).

The catchments of both ice streams comprise large, low-lying (i.e. marine-based) basins extending far into the West Antarctic hinterland (Fig. 1). Pine Island Glacier and TG have small buttressing ice shelves

* Corresponding author at: University of Gothenburg, Department of Marine Sciences, Gothenburg 413 19, Sweden.
E-mail address: patric.simoes.pereira@gu.se (P. Simões Pereira).

https://doi.org/10.1016/j.chemgeo.2020.119649
Received 18 November 2019; Received in revised form 19 April 2020; Accepted 27 April 2020
Available online 05 May 2020
0009-2541/

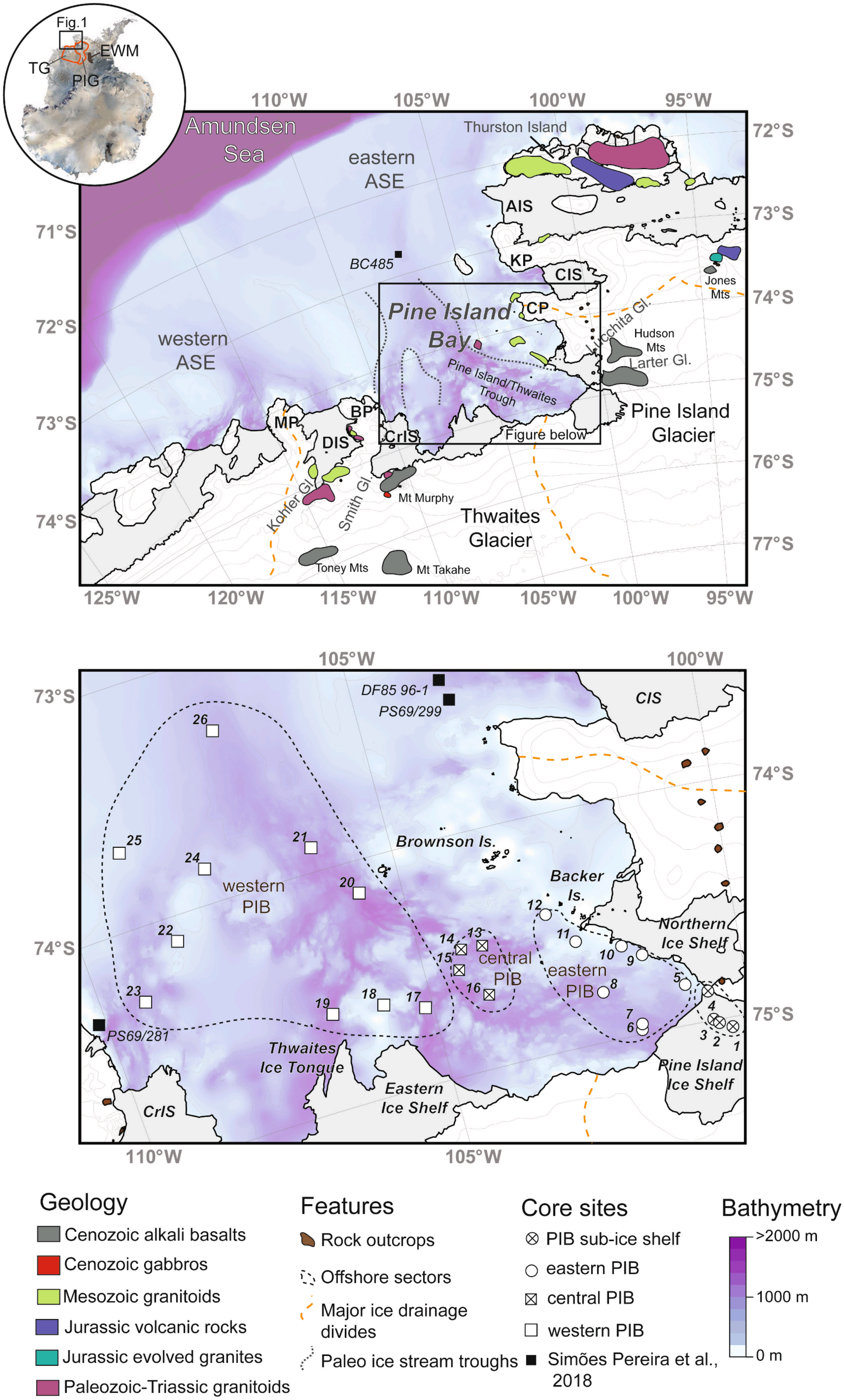

(caption on next page)

Fig. 1. Simplified geological map (top panel) and bathymetric map (top and bottom panel) of the Amundsen Sea sector of West Antarctica, including geological units discussed in the text (Futa and Le Masurier, 1983; Kipf et al., 2012; Pankhurst et al., 1998, 1993; Rocchi et al., 2006). Bathymetry is taken from Arndt et al. (2013). Onshore, major ice divides are shown as orange dashed lines (Zwally et al., 2012) and ice surface 100 m contours are from Fretwell et al. (2013). Sites of seafloor surface sediments analysed in this study are shown as different symbols, and numbers correspond to descriptions provided in Table 1. Additional sites mentioned in the text are from Simões Pereira et al. (2018) and are shown as black squares. Inset: Satellite image of Antarctica, showing the borders of the ice drainage basins of Pine Island Glacier (PIG) and Thwaites Glacier (TG), as well as the location of the Ellsworth-Whitmore Mountains (EWM). ASE: Amundsen Sea Embayment; PIB: Pine Island Bay; AIS: Abbot Ice Shelf, BP: Bear Peninsula, DIS: Dotson Ice Shelf, CIS: Cosgrove Ice Shelf, CP: Canisteo Peninsula, CrIS: Crosson Ice Shelf, KP: King Peninsula, MP: Martin Peninsula.

that are in contact with relatively warm ocean water. Both ice streams are grounded on a bed that deepens further inland, with no physiographic barriers further upstream observed in the TG drainage basin (e.g. Joughin et al., 2009, 2014). Any destabilization in this sector therefore has the potential to result in a run-away retreat of the grounding line further inland (e.g. Schoof, 2007; Joughin et al., 2014).

Alongside other WAIS glaciers draining into the Amundsen Sea Embayment, PIG and TG have been affected by major mass loss over recent decades, expressed by rapid thinning, grounding-line retreat and flow acceleration (e.g. Mouginot et al., 2014; Rignot et al., 2014). Ocean-induced melting at the base of the ice shelves and at the grounding lines has been identified as the main driver of ice loss (e.g. Jacobs et al., 2011; Jenkins et al., 2018), which is presently larger than anywhere else in Antarctica (e.g. Paolo et al., 2015). Melting of glaciers in the Amundsen Sea and the other WAIS sectors has contributed a total of 7.3 mm to global sea-level rise from 1979 to 2017 at an accelerating rate, with PIG and TG alone accounting for ca. 36% of Antarctica's total sea level contribution (Rignot et al., 2019; The IMBIE team, 2018).

Numerical studies suggest that the PIG and TG ice drainage systems collapsed several times over the last 5 Myr (e.g. Pollard and DeConto, 2009; DeConto and Pollard, 2016), but geological evidence for such a collapse during the Late Quaternary is, so far, indirect and mainly based on far-field data, such as sea-level records (e.g. Dutton et al., 2015). Direct geological evidence from records proximal to the WAIS remains elusive. While studies on marine sediment cores from the West Antarctic continental margin could not prove a Late Quaternary WAIS collapse (Hillenbrand et al., 2002, 2009), findings of marine diatoms of Late Quaternary age and elevated beryllium concentrations in subglacial till underlying the Whillans Ice Stream in the Ross Sea drainage sector of the WAIS were interpreted as a result of at least one WAIS collapse during the last 750 ka (Scherer et al., 1998). However, a recent study indicates that the WAIS grounding line had retreated to the sampling site at the beginning of the Holocene (Kingslake et al., 2018), demonstrating that advected marine diatoms and adhering beryllium nuclides might have been carried there by ocean currents, without the requirement for a WAIS collapse.

A major hurdle in identifying ice-sheet collapse in the proxy record of marine sediment cores recovered from the West Antarctic margin is our limited understanding of how exactly such a collapse might be expressed in the sediments (Hillenbrand et al., 2009). A powerful way in which to study past ice dynamics and presence/absence of an eroding ice sheet is to examine the mineralogical and geochemical provenance of the marine sediments deposited at the periphery of the ice sheet (for a recent review see Licht and Hemming, 2017). Subglacial substrate is eroded by ice streams and glaciers, producing glacial detritus, which is transported by ice flow down-stream to the ice-sheet margin. The material carries with it the lithological and geochemical signature of the source rocks and sedimentary strata eroded along the flow line of the ice stream/glacier. At a marine-terminating ice margin the glacigenic detritus can be released in two ways: (i) deposition of unsorted melt-out till directly at the grounding line and deposition from meltwater plumes that emanate from the grounding line, or (ii) deposition further offshore by calved icebergs (e.g. Diekmann and Kuhn, 1999). An important prerequisite for applying mineralogical and geochemical provenance studies back in time (e.g. Ehrmann et al., 1992; Cook et al., 2013; Hillenbrand and Ehrmann, 2002; Pierce et al., 2017; Williams et al., 2010) is the detailed knowledge of the provenance fingerprint of modern continental source areas (Pierce et al., 2014; Simões Pereira et al., 2018).

In this study, we provide the first comprehensive multi-proxy provenance characterization of glacimarine seafloor surface sediments from Pine Island Bay (SE Amundsen Sea Embayment). We identify distinct geochemical fingerprints for two of the most vulnerable Antarctic glaciers, TG and PIG, thereby offering a much-needed framework for studying partial and total WAIS collapse back in time.

2. Regional setting

The bathymetry of the eastern Amundsen Sea Embayment shelf is characterised by a large cross-shelf trough system that extends from the PIG and TG termini to the continental shelf edge, shallowing from ca. 1500 m to 575 m (Fig. 1; Graham et al., 2010; Nitsche et al., 2007). This trough system has been carved into the seabed by past grounded ice stream advances across the shelf (e.g. Graham et al., 2010; Jakobsson et al., 2012). These advances also created an extensive network of subglacial meltwater channels in Pine Island Bay, characterised by a series of interlinked basins eroded into the rugged crystalline bedrock (Lowe and Anderson, 2003; Nitsche et al., 2013; Witus et al., 2014). Along the coastline of the Amundsen Sea Embayment mass loss by iceberg calving is larger than elsewhere around Antarctica (Liu et al., 2015), and rafting of debris by these icebergs is potentially an important transport mechanism that delivers glacial detritus from the coast to the deep sea. Iceberg drift across the Amundsen Sea shelf is generally directed westwards and driven by surface ocean currents, wind and sea-ice drift, with a strong bathymetric control for deep-keeled icebergs (Mazur et al., 2017, 2019).

The geology in the hinterland of the Amundsen Sea Embayment is characterised by variably tectonized calc-alkaline plutonic (granites, granodiorites, tonalites) and volcanic rocks that were emplaced during the long-lived subduction of the (proto-) Pacific plate below the continental margin from the Palaeozoic to Late Cretaceous. Outcrops of such ~90 to ~350 Ma old rocks are observed on Thurston Island, Backer and Brownson islands and onshore of the Dotson Ice Shelf (Fig. 1, upper panel; cf. Kipf et al., 2012; Pankhurst et al., 1993; Riley et al., 2017). In the Jones Mountains, Jurassic granites can be distinguished from other granites in the region by their predominantly silicic (i.e. evolved) composition with higher incorporation of crustal components during magma genesis (Pankhurst et al., 1993). Sporadic outcrops of evolved granites also occur in the Ellsworth-Whitmore Mountains (Fig. 1, inset). Cessation of plate subduction below the margin led to eruption of widespread alkali basalts during the Miocene, which was followed by a phase of felsic volcanism spanning from the Latest Miocene to the Late Quaternary (Hudson Mountains, Mt. Murphy, Mt. Takahe, Toney Mts.; see LeMasurier, 2013). On Dorrel Rock, southwest of Mt. Murphy, a single outcrop composed of a coarse-grained gabbro, which was dated to ca. 34 Ma (amphibole $^{40}Ar/^{39}Ar$ ages; Rocchi et al., 2006), is the only exposed plutonic body related to Cenozoic magmatism. Aeromagnetic and airborne radar investigations have furthermore revealed the presence of large sedimentary basins below PIG and TG (Muto et al., 2016; Schroeder et al., 2014b; Smith et al., 2013) These sedimentary basins were probably formed in association with regional rifting that occurred 90–105 Ma ago, related to

Table 1
Sample location and summary of analytical techniques for provenance tracing (complete dataset is given in Appendix Tables 1, 2).

Number	Sites	Core depth [cm]	Gear[a]	Cruise expedition	Latitude	Longitude	Water depth (m)	Geographical area	Isotopic		Geochemical		$^{40}Ar/^{39}$		Clay mineral assemblages	Rock magnetic properties
									Sr	Nd	Major	Traces	Hornblende (grains)	Biotite (grains)		
1	PIG-B	2	PerC	n.a.	−75.08	−100.43	725	PIG sub-ice shelf	X	X	X	X			X	
2	PIG-A	2	PerC	n.a.	−75.04	−100.65	770	PIG sub-ice shelf	X	X	X	X			X	
3	PIG-C	2	PerC	n.a.	−75.02	−100.70	811	PIG sub-ice shelf	X	X	X	X			X	
4	PS104/008-2	3.5	GC	ANT-XXXII/3	−74.87	−100.71	698	PIG sub-ice shelf	X	X	X	X			X	X
5	PS104/013-2	5	GC	ANT-XXXII/3	−74.84	−101.04	545	Eastern PIB	X	X	X	X			X	X
6	NBP99-02 PC51	17–22	PC	NBP99-02	−74.96	−101.85	998	Eastern PIB		X						
7	PS104/009-1	6	GC	ANT-XXXII/3	−74.99	−101.87	989	Eastern PIB	X	X	X	X	19	10	X	X
8	PS75/159-1	0–1	GC	ANT-XXVI/3	−74.80	−102.36	1046	Eastern PIB	X	X		X	1		X	X
9	PS104/012-2	5	GC	ANT-XXXII/3	−74.68	−101.62	358	Eastern PIB	X	X	X	X			X	X
10	NBP07-02 SMG8	Surface	grab	NBP07-02	−74.62	−101.92	438	Eastern PIB		X						
11	PS75/160-1	1	GC	ANT-XXVI/3	−74.56	−102.62	336	Eastern PIB	X	X	X	X			X	X
12	PS69/288-3	4	GC	ANT-XXIII/3	−74.42	−102.99	772	Eastern PIB	X	X	X	X			X	X
13	PS69/295-1	4	GC	ANT-XXIII/4	−74.48	−104.10	1151	Central PIB	X	X	X	X	6	21	X	X
14	BC476	0–2	BC	JR179	−74.48	−104.42	1120	Central PIB	X	X		X				
15	NBP99-02 53PC	24–29	PC	NBP9902	−74.67	−104.34	1386	Central PIB					15	10		
16	PS69/291-1	7	GC	ANT-XXIII/4	−74.69	−104.16	1023	Central PIB	X	X	X	X	6	12	X	X
17	PS69/292-2	3	GC	ANT-XXIII/4	−74.68	−105.19	1407	Western PIB	X	X	X	X			X	X
18	PS75/167-1[b]	5	GC	ANT-XXVI/3	−74.62	−105.80	526	Western PIB	X	X		X	9		X	X
19	PS75/166-3	6	GC	ANT-XXVI/3	−74.60	−106.64	1385	Western PIB	X	X	X	X			X	X
20	PS75/173-1	5	GC	ANT-XXVI/3	−74.14	−105.73	1507	Western PIB	X	X	X	X	7	10	X	X
21	BC482	0–2	BC	JR179	−73.89	−106.27	1113	Western PIB	X	X		X				
22	NBP07-02 SMG10	Surface	grab	NBP07-02	−74.10	−108.61	730	Western PIB		X						
23	NBP00-01 KC28	9–14	GC	NBP00-01	−74.30	−109.36	1012	Western PIB		X						
24	PS75/177-1	5	GBC	ANT-XXVI/3	−73.85	−107.88	740	Western PIB	X	X	X	X	10	24	X	X
25	PS75/219-2	3	GBC	ANT-XXVI/3	−73.67	−109.00	458	Western PIB	X	X	X	X			X	X
26	PS104/021-1	5	GC	ANT-XXXII/3	−73.30	−107.11	882	Western PIB	X	X	X	X			X	X

[a] PerC: percussion corer; GC: gravity corer; PC: piston corer; grab: Smith-Mcintyre Grab; GBC: giant box corer.
[b] Proximal to site PS75/168-1.

plate reorganization within West Antarctica (Jordan et al., 2010).

3. Samples

Here we present geochemical and mineralogical compositions, and magnetic properties of seafloor surface sediment samples recovered from 26 sites in Pine Island Bay (Fig. 1, lower panel; Table 1). Three cores from below the (central) PIG Ice Shelf and 23 cores from seasonal open marine shelf areas were sampled due to their proximity to PIG, TG and smaller ice streams in the region, e.g. Lucchitta Glacier and Larter Glacier that flow through the Hudson Mountains and feed into the Northern Ice Shelf (Johnson et al., 2014; Rignot, 2002). The Northern Ice Shelf was connected to the PIG Ice Shelf and our site 4 was ice-shelf covered until 2015 (Jeong et al., 2016; Arndt et al., 2018), but now site 4 is seasonally ice-free and open marine. Furthermore, Haynes Glacier, Pope Glacier and Smith Glacier drain into the south-western Pine Island Bay, with the latter two ice streams feeding into the Crosson Ice Shelf (Rignot et al., 2014; Scheuchl et al., 2016) (Fig. 1; Figure simplified to show Smith Glacier only).

We divided the studied sites into four groups based on their geographical locations: PIG sub-ice shelf (n = 4, including site 4), eastern Pine Island Bay (n = 8), central Pine Island Bay (n = 4), and western Pine Island Bay (n = 10).

Sub-ice shelf sediments deposited on a prominent ridge below the PIG ice shelf were retrieved with a hand-operated percussion corer after hot-water drilling through the ice shelf (Smith et al., 2017). Offshore sediment samples were collected using gravity, (giant) box and piston corers as well as sample grabs during a number of shipborne expeditions to the area conducted by the Alfred Wegener Institute (Germany), the British Antarctic Survey (UK) and the U.S. Antarctic program (see Table 1 for full list). All surface sediments consist of laminated to homogenous or bioturbated terrigenous muds and sandy muds described from offshore sites elsewhere in Pine Island Bay (Hillenbrand et al., 2013, 2017; Kirshner et al., 2012; Nitsche et al., 2013; Smith et al., 2014, 2017; Witus et al., 2014). We infer a modern or late Holocene age for the near surface sediments based on their composition, stratigraphic position and AMS ^{14}C and ^{210}Pb dating of similar sediments in the eastern Amundsen Sea Embayment (Hillenbrand et al., 2013, 2017; Klages et al., 2013, 2017; Larter et al., 2014; Smith et al., 2014, 2017; Witus et al., 2014).

4. Methods

We applied a multi-proxy toolbox to characterise seafloor surface sediments and derive their provenance. Our investigations included analyses of detrital Sr and Nd isotope, and major and trace element compositions of the fine-grained fraction (< 63 μm), ^{40}Ar/^{39}Ar dates on coarse (> 150 μm) hornblende and biotite grains, mineral composition of the clay fraction (< 2 μm) and rock magnetic parameters of the bulk sediment. All methods are described below. Note that not all methods were applied at each site (cf. Table 1 and Appendix Tables 1, 2).

4.1. Strontium and neodymium isotope composition

Bulk sediment samples (~10 cc) were freeze-dried and sieved into < 63 μm, 63–150 μm and > 150 μm fractions. An aliquot (~500 mg) of the fine-grained (< 63 μm) fraction was sequentially leached to remove biogenic carbonate using buffered acetic acid and authigenic ferromanganese coatings using a 0.02 M hydroxylamine hydrochloride solution, following the procedure by Rutberg et al. (2000), based on Chester and Hughes (1967). No removal of biogenic opal was conducted, which is an insignificant carrier of trace elements (Collier and Edmond, 1984). Grousset et al. (1998), for example, reported Sr and Nd concentrations in biogenic opal of ~5 ppm and ~3 ppm, respectively (see also Bayon et al., 2002). Furthermore, seafloor surface sediments in Pine Island Bay are mainly terrigenous, and microfossil content (incl. diatoms) is known to be very low (e.g. Kellogg and Kellogg, 1987). After homogenization of the leached and dried sediment, approximately ~50 mg of the residual (detrital) fraction were weighted into Savillex beaker and dissolved using a mixture of 2 ml of HF (27 M), 1 ml of HNO_3 (15 M) and 0.8 ml of $HClO_4$ (20 M) for three to four days on a hotplate until no visible particles remained. Strontium and Nd fractions were purified using a three-stage ion-exchange chromatography. The first column utilised cation-exchange resin, AG50W-X8, and hydrochloric acid in different molarities, to separate Sr and the rare earth elements (including Nd) from the sample matrix. The Sr fraction was subsequently purified using Eichrom's Sr spec (modified from Pin and Bassin, 1992), while Nd was separated from the other rare earth elements using Ln-Spec resin (50–100 μm; modified from Pin and Zalduegui, 1997).

Dried Sr cuts were re-dissolved in 10 μl HCl, and a 1 μl aliquot was loaded onto degassed tungsten filaments with 1 μl of $TaCl_5$ activator. Strontium isotope ratios were measured in static mode on a TRITON thermal ionisation mass spectrometer (TIMS) at the MAGIC laboratories at Imperial College London using virtual amplifier rotation. Raw ^{87}Sr/^{86}Sr ratios were corrected for mass bias by normalizing to an ^{88}Sr/^{86}Sr ratio of 8.375 using an exponential law. Samples were analysed in three batches between February 2017 and January 2018 during which time the SRM987 standard yielded a ^{87}Sr/^{86}Sr ratio of 0.710250 ± 0.000010 2.S.D. (n = 39). For consistency with published ratios, results reported in Appendix Table 1 were corrected to the accepted value of 0.710252 ± 0.000013 (Weis et al., 2006). Three separate digestions of USGS standard BCR-2 gave an ^{87}Sr/^{86}Sr ratio of 0.705015 ± 0.000010 2.S.D. (n = 3), within error the same as the accepted value of 0.705013 ± 0.000010 2.S.D. reported by Weis et al. (2006). Procedural blanks were ~100 pg, 104 pg and ~ 900 pg.

Neodymium isotope compositions were measured on a Nu Instruments multi-collector inductively coupled plasma mass spectrometer (MC-ICP-MS) in the MAGIC facilities at Imperial College London. The Nd isotope ratios were obtained after correcting for instrumental mass bias using a ^{146}Nd/^{144}Nd ratio of 0.7129 and an exponential law. Sample results reported in Appendix Table 1 were obtained during four measurement sessions over a period of three months. For three batches, reported ^{143}Nd/^{144}Nd ratios were corrected using the offset of the average ^{143}Nd/^{144}Nd JNdi ratio of the run (0.512137 ± 0.000011, n = 20; 0.512119 ± 0.000015, n = 28; 0.512117 ± 0.000013, n = 17) relative to the accepted ratio of 0.512115 ± 0.000007 (Tanaka et al., 2000). For one batch, we applied a correction using the two bracketing standards due to a drift in the observed ^{143}Nd/^{144}Nd JNdi ratio. Reported external errors for this batch of samples were based on the largest BCR-2 ^{143}Nd/^{144}Nd offset to the accepted value of 0.512638 ± 0.000015 (Weis et al., 2006). Inter-batch comparison of repeat sample analysis showed that Nd isotope compositions always reproduced within their respective error bars. Neodymium blanks were unusually high with 150, 210, 1260 pg, but still only accounted for < 0.5% of the sample signal. Mass balance calculation confirmed that blanks were negligible due to the large amount of sample processed.

4.2. Major and trace element compositions

An additional split (~50 mg) of the leached < 63 μm residual was separately digested for major and trace element analysis using the same method detailed above. After conversion to nitrate form, solutions were taken to the Open University in Milton Keynes. Analysis of major and trace element composition were performed on an Agilent 8800 ICP-QQQ, an inductively coupled plasma mass spectrometer with an integrated collision/reaction cell to remove targeted interference ions. Most elements were measured with no gas or He gas in the collision reaction cell, except for rare earth elements measured with O_2. Oxide formation (CeO^+/Ce^+) was kept below 1.0% and 0.6% in no gas and He gas mode, respectively, and doubly charged species (Ce^{2+}/Ce^+) were kept below 1.5% and 1.0%, respectively. Analyses were standardized against five USGS reference materials, in addition to an internal standard to correct for instrument drift. Detection limits of light trace elements were typically 2–50 ppt in solution, while mid to heavy trace elements (Rb-U) were ≤ 2 ppt. Repeated BCR-2 standard measurements ($n = 11$) indicate an overall precision for trace elements better than 5%, with accuracy better than 10%. Major element precision and accuracy was ~5%.

4.3. Clay mineralogy

Sediment samples (~10 cc) were processed and analysed for clay mineral assemblages at the Institute for Geophysics and Geology, University of Leipzig (Germany), following standard procedures (see Ehrmann et al., 1992, 2011, and references therein). A split (~1 g) of the fine-grained (<63 μm) sample (sieved during sample processing for Sr and Nd isotope analysis) was repeatedly leached with acetic acid (10%) and H_2O_2 to remove carbonate and the organic fraction. The clay fraction (<2 μm) was separated from the remaining sample in settling tubes after being mixed with an internal MoS_2 standard at a ratio of 0.4 to 1. The suspended material was rapidly filtered through a 0.2 μm membrane filter to obtain a texturally oriented aggregate, and then dried and fixed on small aluminium tiles with exposure to ethylene glycol vapour (60 °C for 18 h) before X-ray diffraction analysis. Diffractograms were obtained using a Rigaku New Miniflex diffractometer with CoKα radiation (30 kV, 15 mA) by irradiating the range of 3–40° 2Θ (at 0.02° 2Θ steps/4 s integration time), and again the range of 27.5–30.5° 2Θ (0.01° 2Θ steps/4 s integration time) to better discriminate the kaolinite (002) peak from the chlorite (004) peak. Diffractograms were assessed using "MacDiff" (Petschick et al., 1996). Diffraction patterns were adjusted for the MoS_2 peak (6.15 Å) and clay groups were identified based on their basal reflections at 16.5 Å for smectite (after glycolization), at 10 Å for illite, 3.58 Å for kaolinite and 3.54 Å for chlorite. Semi-quantitative analyses were measured using empirically determined weighing factors on the integrated peak areas of the different clay mineral groups (Biscaye, 1964, 1965).

4.4. $^{40}Ar/^{39}Ar$ ages of individual iceberg-rafted hornblende and biotite grains

Individual hornblende and biotite grains were picked from the coarse (>150 mm) size fraction, which is a reliable proxy for iceberg-rafted debris (IRD; e.g. Diekmann and Kuhn, 1999) and were analysed for their $^{40}Ar/^{39}Ar$ ages. The differences in closure temperature of hornblende and biotite grains (~550 and 300 °C, respectively) and their different fertility in certain lithologies (e.g., Pierce et al., 2014; Licht and Hemming, 2017), make them complementary in tracing source terrains. Sample and monitor (Fish Canyon sanidine) grains were irradiated at the TRIGA reactor at the USGS in Denver, Colorado (U.S.A.). The neutron flux was calibrated using J-values calculated to normalize Fish Canyon sanidine grains to 28.201 ± 0.046 Ma (Kuiper et al., 2008). Subsequent $^{40}Ar/^{39}Ar$ age measurements were carried out using single-step CO_2 laser-fusion at the Lamont-Doherty Earth Observatory Argon Geochronology for the Earth Sciences (AGES) laboratory (U.S.A.), after correcting for atmospheric argon ($^{40}Ar/^{36}Ar = 298.6$; Lee et al., 2006), procedural blanks, mass discrimination and nuclear interferences (Dalrymple et al., 1981).

4.5. Rock magnetic properties

Samples for rock magnetic investigations were collected in small oriented cubes of 6.2 cm^3 pushed into the split core section. Low-field magnetic susceptibility (MS), anhysteretic remanent magnetization and its median destructive field (ARM and MDF_{ARM}, respectively) and isothermal (IRM) remanent magnetization were measured with an automated 2G SQUID Rock Magnetometer at the Department of Earth Sciences, University of Bremen (Germany). ARM was imparted in a peak alternating field of 100 mT and a DC bias field of 50 μT, and the samples were subjected to alternating field demagnetization applying 16 steps with 5 mT increment between 0 and 50 mT, and 10 mT increment between 60 and 100 mT peak field. While virtually all minerals contribute to the measured MS, ARM usually quantifies the content of fine-grained (<1 μm) stable single-domain (SSD) and pseudo single domain magnetite (Banerjee et al., 1981; Frederichs et al., 1999). The MDF_{ARM} is the alternating field demagnetization level at which the intensity of the ARM is reduced by one half. Anhysteretic susceptibility (κ_{ARM}) was calculated by dividing the intensity of ARM given in A/m by the DC bias field of 50 μT. κ_{ARM} was divided by magnetic volume susceptibility (both are dimensionless) to calculate the ratio κ_{ARM}/κ. IRM was imparted in DC fields up to 700 mT applying increments of 5 mT between 0 and 50 mT field strength, 10 mT between 60 and 100 mT and 25 mT between 125 and 200 mT. Additional steps used fields of 250, 300, 500 and 700 mT. IRM_{100mT} is dependent on the content of coarser-grained minerals with coercivities below 100 mT, typically (titano) magnetite, meaning that the ratio ARM_{100mT}/IRM_{100mT} can be used as a magneto-granulometric index with higher values indicating smaller particles (King et al., 1982). Saturation IRM (SIRM) and hard IRM (HIRM) provide estimates of the content of high-coercivity anti-ferromagnetic minerals, such as hematite and goethite, in the samples. The S-ratio ($S = 0.5 \cdot [(-IRM_{-300mT}/SIRM) + 1]$) represents the ratio of low to high-coercive magnetic minerals (e.g. magnetite vs. hematite) (Bloemendal et al., 1992).

5. Results

Our new dataset is complemented by previously published data from Pine Island Bay (Ehrmann et al., 2011; Simões Pereira et al., 2018; Smith et al., 2017). Results are illustrated in Figs. 2 to 5 and Appendix Fig. 1. The full dataset is based on seafloor surface sediment samples from 26 sites, including the previously analysed samples, and consists of strontium and neodymium isotope (21 and 25 samples, respectively), major (17 samples) and trace element (21 samples) compositions of fine-grained sediments, as well as $^{40}Ar/^{39}Ar$ ages of individual iceberg-rafted hornblende and biotite grains (160 grains from 8 samples), clay mineral compositions (19 samples) and rock magnetic properties of bulk sediment fractions (16 samples).

5.1. Strontium and neodymium isotope compositions and clay mineral assemblages

The Sr and Nd isotope compositions and clay mineral signatures of seafloor surface sediments in Pine Island Bay fall between two end-members: the PIG sub-ice shelf samples and the sample from site 19 located directly offshore from the Thwaites ice tongue (Figs. 2, 3; Appendix Fig. 1). The PIG sub-ice shelf samples record the lowest Nd and highest Sr isotope values (ε_{Nd}: −9.1 to −8.3; $^{87}Sr/^{86}Sr$: 0.7265 to 0.7305) in Pine Island Bay. These samples are further characterised by low smectite (~7%) and low kaolinite content (14–18%), as well as low smectite/illite (~0.1) and kaolinite/illite ratios (0.3) when compared to other samples from the area. Across Pine Island Bay, a general east-west trend in radiogenic isotopes and clay mineralogy can be observed: Neodymium isotope compositions become progressively more radiogenic towards the west (eastern Pine Island Bay: $\varepsilon_{Nd} = -8.3$ to -6.7; omitting site 10; central Pine Island Bay: $\varepsilon_{Nd} = -6.0$ to -5.9; western Pine Island Bay: $\varepsilon_{Nd} = -5.1$ to -2.3), while Sr isotope ratios show the opposite trend (eastern Pine Island Bay: $^{87}Sr/^{86}Sr$: 0.7240 to 0.7181; central Pine Island Bay: $^{87}Sr/^{86}Sr$: 0.7191 to 0.7173; western Pine Island Bay: $^{87}Sr/^{86}Sr$: 0.7169 to 0.7128). Smectite and kaolinite contents, and particularly the smectite/illite and kaolinite/illite ratios, also show an increase from the east (PIG sub-ice shelf samples: smectite/illite ~0.10 and kaolinite/illite ~0.28) to the west (site 19: smectite/illite ~0.56 and kaolinite/illite ~1.04). Sites 22 and 23, which are located in the vicinity of a minor bathymetric trough that extends NNE-wards

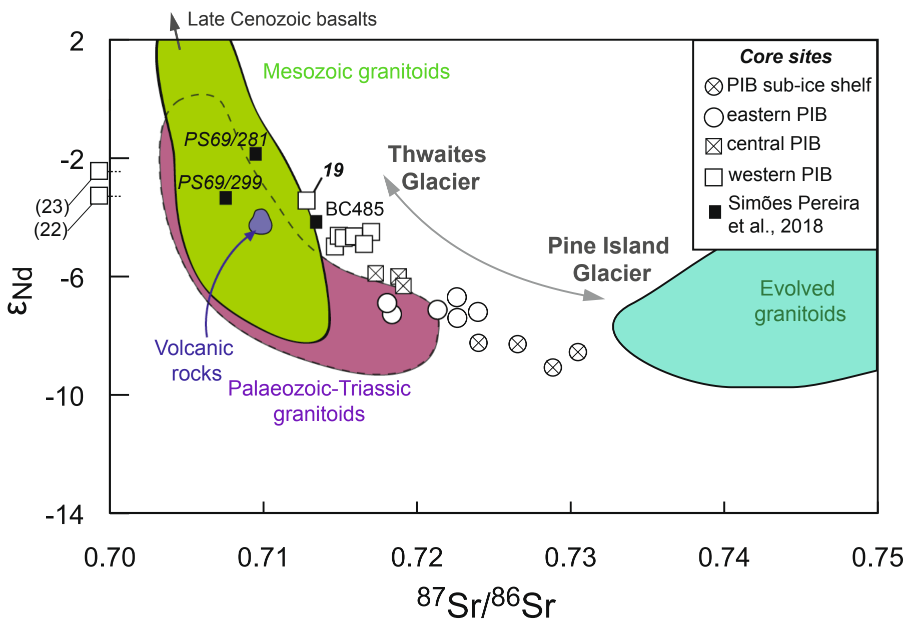

Fig. 2. Neodymium and strontium isotope compositions of detrital seafloor surface sediments in Pine Island Bay. Symbols and site numbers according to Fig. 1 and Table 1. Note that for sites 22 and 23 only the Nd isotopic composition is available. Isotopic composition of major bedrock outcrops shown in Fig. 1 from Simões Pereira et al. (2018). Source data on Jurassic volcanic rocks from Thurston Island refer to two samples from Pankhurst et al. (1993) and Riley et al. (2017), respectively.

from the westernmost Crosson Ice Shelf (Fig. 1; unnamed trough), are characterised by the highest ε_{Nd} values of western Pine Island Bay ($\varepsilon_{Nd} = -3.4$ and -2.3, $n = 2$).

5.2. Iceberg-rafted hornblende and biotite grains

Iceberg-rafted debris from eastern Pine Island Bay (2 samples; 30 grains) is characterised by predominant ages between 170 and 270 Ma ($n = 25$) (Figs. 4, 5). This age range is absent or at least much less pronounced in other sectors in Pine Island Bay. In contrast, iceberg-rafted debris from central Pine Island Bay (3 samples, 70 grains) yielded predominant ages from 90 to 160 Ma ($n = 56$), with two major age peaks at ~100 and 115 Ma, as well as minor age populations from 180 to 270 Ma ($n = 9$) and from ~0 to 60 Ma ($n = 5$). Iceberg-rafted debris at sites in western Pine Island Bay (3 samples, 60 grains) contains a high number of hornblende and biotite grains between 110 Ma and 380 Ma old ($n = 52$), with a predominant age peak at ~115 Ma. These sites also contain a noticeable number of grains younger than 40 Ma ($n = 6$).

Hornblende and biotite grains have been observed in all seafloor surface sediment samples from Pine Island Bay and show similar age distributions (Appendix Table 2). The only exception to this general observation is the sample from site 20. Here biotite ages are 110–200 Ma ($n = 10$) and hornblende ages are predominantly 250–380 Ma ($n = 6$). However, nearby sites (i.e. sites 18 and 24) in western Pine Island Bay show presence of both, hornblende and biotite grains in the 110–200 Ma and 250–380 Ma age intervals. We therefore suggest that the apparent age difference between biotite and hornblende grains at site 20 is unlikely to bear any geological meaning.

5.3. Statistical analysis map based on major and trace elements, clay minerals and rock magnetics

We calculated a Principal Component Analysis (PCA) map using the software package 'provenance' (Vermeesch et al., 2016) in order to extract meaningful information from the large datasets produced by our multi-proxy provenance analysis (Fig. 6). Trace elements selected were those with predominantly detrital signatures (Ti, Y, Zr, Nb, Hf) and those likely to be representative of source rock composition (Sc, V, Co, Ni, Rb, Sr, Th, U) (Pe-Piper et al., 2008). Of the rare earth elements only La, Yb, and Lu were selected. Furthermore, we included the anhysteretic remanent magnetization (ARM), which is a proxy for relative

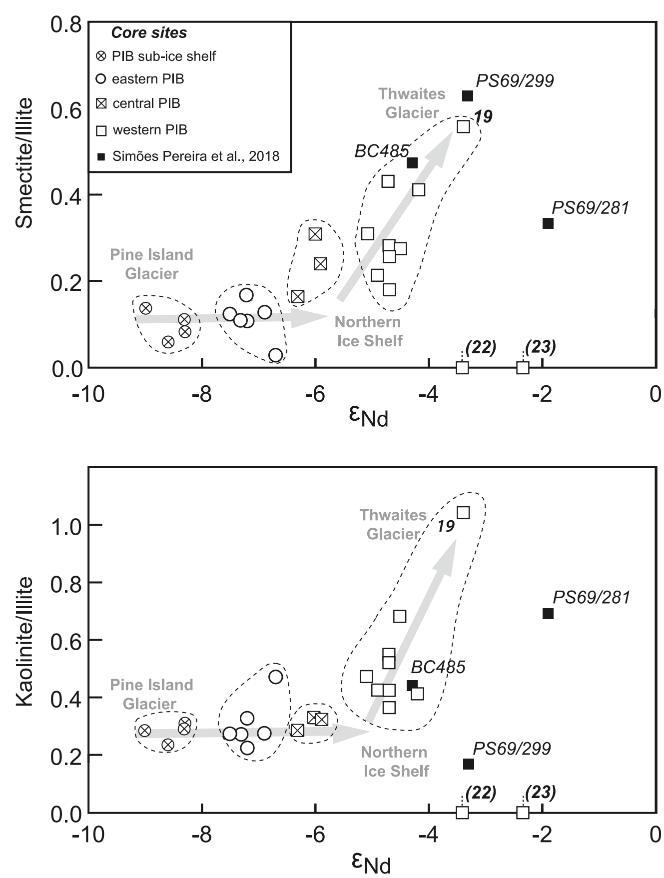

Fig. 3. Neodymium isotope composition of <63 µm detrital seafloor surface sediments vs smectite/illite (upper panel) and kaolinite/illite (lower panel) ratios from the <2 µm fraction in the same samples. Symbols and site numbers according to Fig. 1 and Table 1. Note the consistent trend from Pine Island Glacier and eastern Pine Island Bay towards western Pine Island Bay and site 19 located proximal to the Thwaites Ice Tongue (Fig. 1). No clay mineral data are available for sites 22 and 23.

abundance of fine-grained magnetite, hard isothermal remanent magnetization (HIRM), a proxy for high-coercive minerals such as goethite and hematite, ARM/IRM, an indicator of magnetic grain size variations,

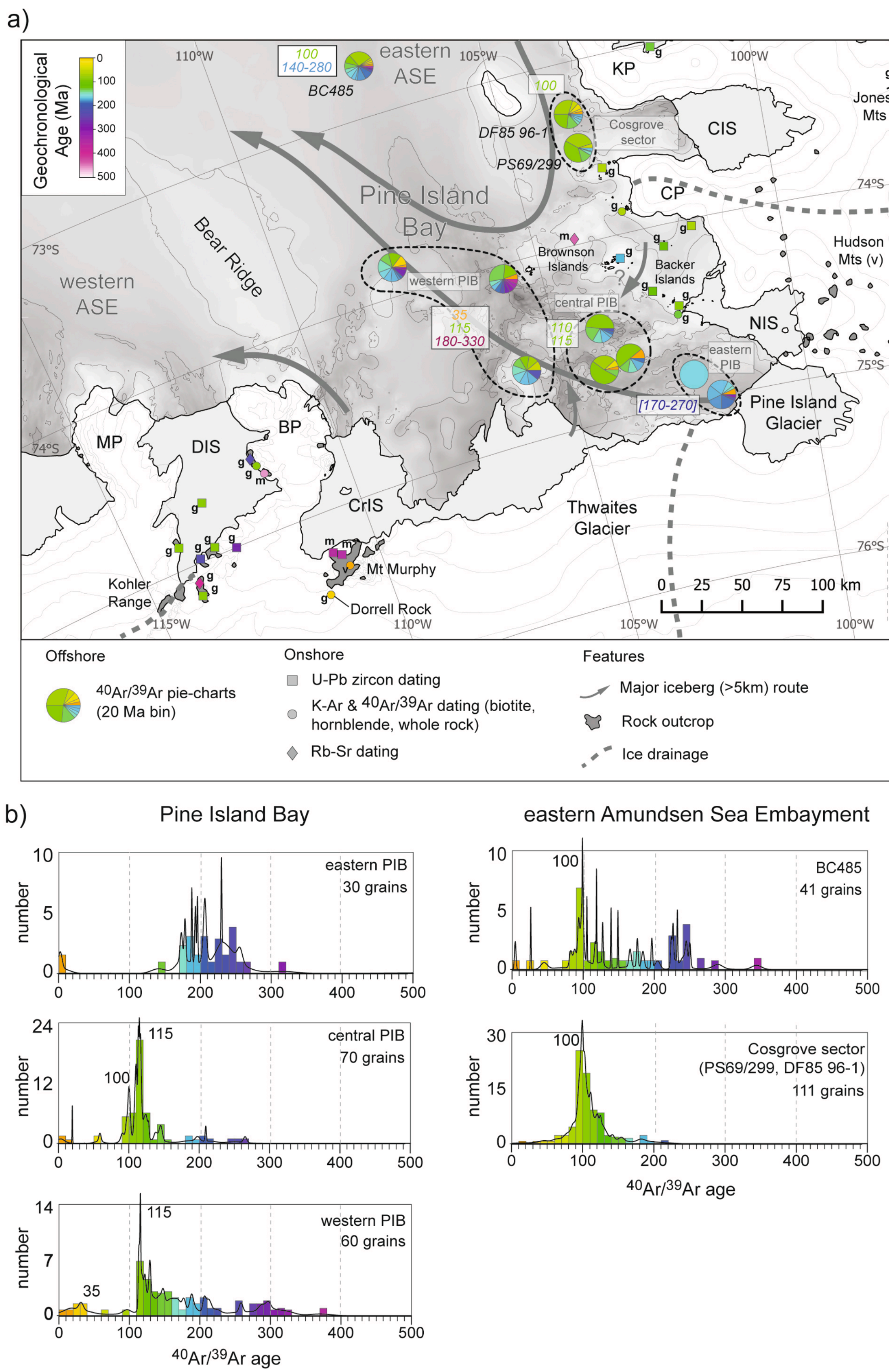

(caption on next page)

Fig. 4. a) Overview map, Pine Island Bay. Offshore pie charts represent thermochronological $^{40}Ar/^{39}Ar$-ages of iceberg-rafted hornblende and biotite grains in surface sediments in 20 Myr increments. Ages for outcrops on land are displayed with different symbols depending on the type of dated mineral and the dating method (based on Simões Pereira et al., 2018). Letters mark rock types which were dated (g = granitoids, m = metamorphic rocks, v = volcanic rocks). Map shows bathymetry and altitude, respectively, in 100-m contour lines. Arrows illustrate general iceberg pathways. b) $^{40}Ar/^{39}Ar$ ages of hornblende and biotite grains from the three sectors in Pine Island Bay discussed in the text. Additional result histograms for site BC485 and samples from the Cosgrove Ice Shelf sector are shown for comparison (Simões Pereira et al., 2018). Histograms are produced using 10 Ma as bin intervals. Probability density plots were calculated using ISOPLOT4.15 (Ludwig, 2003). ASE: Amundsen Sea Embayment; PIB: Pine Island Bay; BP: Bear Peninsula, CIS: Cosgrove Ice Shelf, CP: Canisteo Peninsula, CrIS: Crosson Ice Shelf, DIS: Dotson Ice Shelf, KP: King Peninsula, MP: Martin Peninsula, NIS: Northern Ice Shelf.

and low-field magnetic susceptibility (Liu et al., 2012).

The two first principal components PC1 and PC2 of our selected dataset account for ~69% of the total variance, with the 1st axis PC1 constituting 48% and the 2nd axis PC2 constituting 21% of the variance. Overall, results are clustered within different groups that match the geographical locations of the sites (see Fig. 1), with site 4 (sub-ice shelf) and site 19 (in front of TG, western Pine Island Bay) displaying contrasting loadings on the 1st axis.

6. Discussion: Provenance of modern-Late Holocene detrital sediments in Pine Island Bay

6.1. Geochemical and clay mineralogical signature of fine-grained detritus

Seafloor surface sediments in Pine Island Bay show significant and systematic compositional variation with geographical position. Glacially eroded fine-grained detritus delivered offshore by PIG is characterised by low ε_{Nd} values (~ −9), high $^{87}Sr/^{86}Sr$ (~0.7275) ratios, as well as relatively low smectite/illite (0.1) and kaolinite/illite ratios (~0.3), and thus possesses a distinct provenance fingerprint that allows us to differentiate it from glacimarine sediments supplied from other ice streams draining into Pine Island Bay and the wider Amundsen Sea Embayment. This distinctive signature is most prominent in the surface sediments below the PIG ice shelf. Based on the isotopic composition of seafloor surface sediments deposited at site 8 (PS75/159-1), Simões Pereira et al. (2018) suggested that the substrate below the PIG drainage basin is composed of a mixture of evolved Jurassic granites and Palaeozoic-Mesozoic granitoids of calc-alkaline composition. Nearby outcrops of the former rocks are found in both the Jones Mountains (Fig. 1, upper panel) and the Ellsworth-Whitmore Mountains (inset Fig. 1, upper panel; Craddock et al., 2017), and outcrops of the latter rocks are widespread along the Amundsen Sea coast (Kipf et al., 2012; Mukasa and Dalziel, 2000; Pankhurst et al., 1993, 1998). Our previous interpretation is supported by the new data, which reveal that the Sr and Nd isotope signatures of the PIG sub-ice shelf samples fall in between the signatures of the evolved Jurassic granites and the Palaeozoic-Mesozoic granitoids (Fig. 2), indicating that sub-ice shelf sediments represent a mixture of these two sources. In contrast, a volcanic source, similar to the Jurassic volcanic rocks on Thurston Island and the Cretaceous volcanic rocks in the Jones Mountains (Fig. 1, upper panel; Pankhurst et al., 1993; Riley et al., 2017), can be ruled out because smectite, which is produced by weathering of volcanic detritus (Ehrmann et al., 1992), is low in the PIG sub-ice shelf samples (cf. Smith et al., 2017). Our data, however, do not reveal whether the sub-ice shelf samples consist of subglacial detritus, which had been eroded relatively recently from distinct outcrops of evolved Jurassic and Palaeozoic granitoids under the modern ice stream and subsequently were mixed within the till bed during subglacial transport along the flow line. Alternatively, the sub-ice shelf samples could reflect direct supply from a sedimentary basin further upstream (Smith et al., 2013) that comprises sedimentary strata derived from these two major lithologies.

The isotope signature of sediments becomes more radiogenic (ε_{Nd}: ~ −8.0 to ~ −6.7; $^{87}Sr/^{86}Sr$: 0.7234 to 0.7181) immediately offshore from the PIG ice shelf front, i.e. in eastern Pine Island Bay (Fig. 2). However, clay mineral ratios and assemblages remain relatively uniform between the sub-ice shelf environment of PIG and the proximal marine realm (e.g. smectite/illite: ~0.1; kaolinite/illite: ~0.3) (Fig. 3). The most plausible explanation for this local decoupling between geochemical and mineralogical provenance of fine-grained detritus is that sites in eastern Pine Island Bay receive an additional input of detritus supplied by ice feeding into the Northern Ice Shelf (Fig. 1). Given the

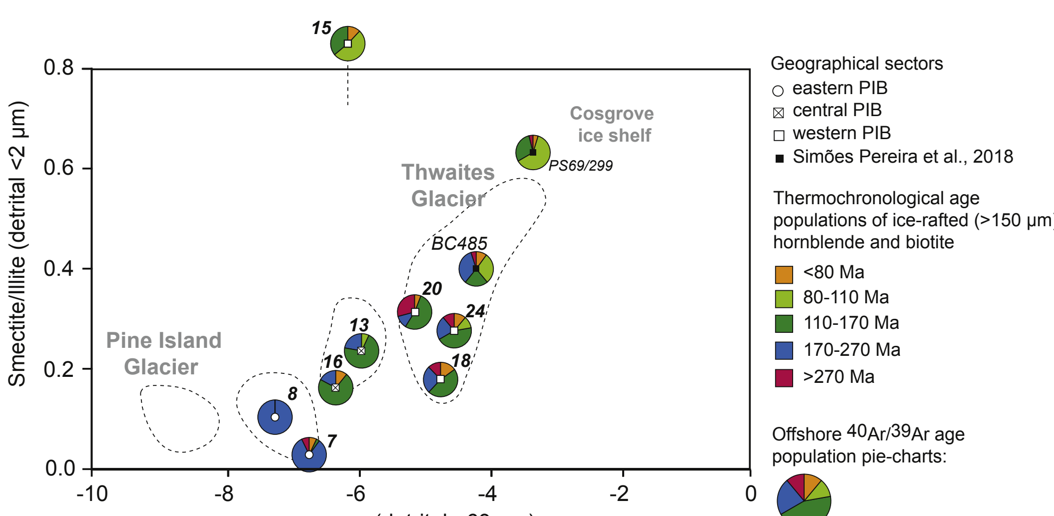

Fig. 5. Comparison of Nd isotope compositions of detrital sediments (< 63 µm) and smectite/illite ratio on the clay fraction (< 2 µm) as well as $^{40}Ar/^{39}Ar$ age populations of iceberg-rafted hornblende and biotite grains (> 150 µm). The latter are illustrated as coloured pie charts based on different age groups. Symbols in the centres of the pie charts mark geographical locations of the samples (Fig. 1). Stippled lines encircle samples from the same sectors as illustrated in Fig. 3. Note that bins for $^{40}Ar/^{39}Ar$ ages are different from those shown in Fig. 4. At site 8 only a single grain could be analysed. No clay mineral data are available for site 15. (For interpretation of the references to colour in this figure legend, the reader is referred to the web version of this article).

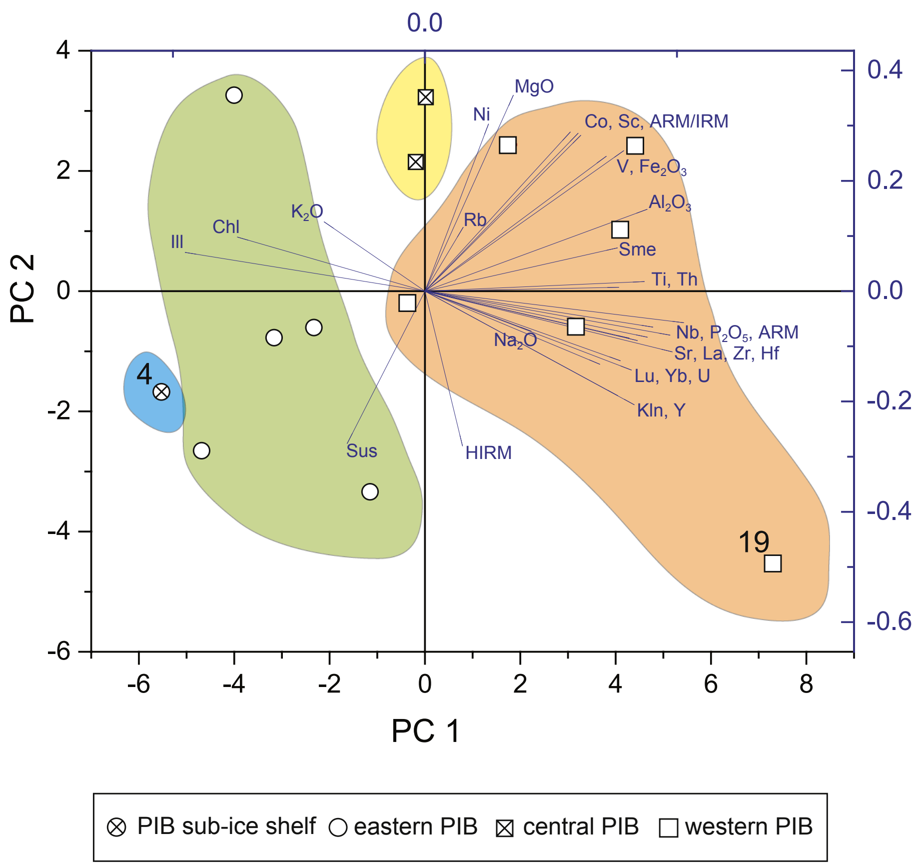

Fig. 6. Principal component analysis (PCA) based on selected elemental, clay mineral and rock magnetic datasets (indicated by blue lines, see text for further discussion). Coloured fields group the different geographical sectors discussed in text and illustrated in the same colours in Fig. 7. Field colour was chosen arbitrary and does not relate to previous figures. For simplification, only sites 4 and 19 are displayed by number on the PCA map. (For interpretation of the references to colour in this figure legend, the reader is referred to the web version of this article).

different grain-sizes of the fractions utilised for clay mineral analysis (<2 μm) and geochemical analysis (<63 μm), we conclude that the glaciers flowing into the Northern Ice Shelf supply silt-sized (2–63 μm) glacial flour, produced through comminution by ice crushing (e.g. Boulton, 1996), with higher ε_{Nd} values compared to those of material delivered by PIG. Low smectite content of ~6% in seafloor surface samples from eastern Pine Island Bay rule out significant contribution from volcanic sources, such as the Late Miocene-Pliocene volcanic rocks cropping out in the Hudson Mountains (Rowley et al., 1990). They support the idea that bedrock upstream of the Northern Ice Shelf consists mainly of Palaeozoic to Mesozoic granitic rocks, which crop out locally on the Backer and Brownson islands and on Canisteo Peninsula and King Peninsula (Pankhurst et al., 1998) (see Fig. 1 for locations).

The geochemical and clay mineral signature of seafloor surface sediments changes from east to west towards a signature comparable to that of the sample from site 19, seaward of the Thwaites Ice Tongue. This trend can be interpreted as two-component mixing of sediments from eastern Pine Island Bay and detritus supplied by TG. Kaolinite in Pine Island Bay sediments has been suggested to be mainly sourced from TG (Ehrmann et al., 2011) likely as a result of erosion of pre-Oligocene sedimentary strata in the Byrd Subglacial Basin and/or Bentley Subglacial Trench (Hillenbrand et al., 2003), located upstream in the WAIS interior (Fretwell et al., 2013). Our data confirm this idea and further suggest that TG is a major source of smectite, as indicated by smectite content as high as 20% at site 19. Sources for this clay mineral are typically volcanic rocks, which have been inferred to lie below the TG drainage basin (Behrendt, 2013; van Wyk de Vries et al., 2017). There are, however, no known outcrops within the TG catchment, rendering exact interpretation of geological sources difficult (see also Section 6.1.2).

6.2. Sources for iceberg-rafted hornblende and biotite grains and insights from statistical analysis maps

$^{40}Ar/^{39}Ar$ ages in IRD from central and western Pine Island Bay are clearly distinct from those in eastern Pine Island Bay, with the former showing well-defined ~100 and ~ 115 Ma age peaks. We relate the ~100 Ma age peak in central Pine Island Bay to a rock source located on the eastern coast of the Amundsen Sea Embayment (i.e. ages match the previously observed $^{40}Ar/^{39}Ar$ age peak offshore from the Cosgrove Ice Shelf; Figs. 4, 5). This is supported by recently published iceberg trajectories, documenting that icebergs calved along this coast drift SSW-wards into central PIB before turning westwards (Mazur et al., 2019). However, given the proximity of the central and western Pine Island Bay sites to TG, we suggest that the dominant ~115 Ma age peak in IRD in these two sectors is sourced from the TG catchment (Fig. 4), and that the TG catchment is underlain by igneous rocks with similar crystallization and/or cooling ages as the rocks cropping out upstream of the Dotson and Crosson ice shelves (Fig. 4).

The predominant Cretaceous age peak of ~115 Ma observed in the new IRD results from glacimarine seafloor surface sediments in western and central Pine Island Bay matches the timing of episodic magmatic flare-ups that occurred in other parts of West Antarctica between 100 and 130 Ma (Antarctic Peninsula: U-Pb zircon, Ar-Ar, K-Ar; Rb-Sr; Riley et al., 2018). The mid-Cretaceous was characterised by rapid emplacement of huge granodiorite-tonalite batholiths along the active margin of West Gondwana (Riley et al., 2018), caused by plate reconfiguration or plume-lithosphere interaction. Similarity between the new IRD ages and onshore geochronology points towards continuation of the Cretaceous orogenic belt to the eastern Amundsen Sea Embayment beneath the Thwaites Glacier catchment. Icebergs released by PIG and TG into eastern, central and western Pine Island Bay travel initially NNW-wards, but when they reach the outer shelf, i.e. the area north of ca. 73° S, they turn westwards and continue to drift in a westerly direction across the shelf (Mazur et al., 2019). In contrast, icebergs sourced from the Dotson and Crosson ice shelves are directed westwards immediately after calving (Mazur et al., 2019), ruling out eastward transport of IRD from there (Fig. 4).

The $^{40}Ar/^{39}Ar$ age populations of hornblende and biotite grains in eastern Pine Island Bay record notable Jurassic to Triassic (~180–250 Ma) cooling ages (Figs. 4, 5), matching closely the ages of Latest Triassic to Jurassic granites cropping out in the Jones Mountains (183 Ma K-Ar muscovite; Pankhurst et al., 1993), on the Brownson Islands (194 Ma U-Pb zircon; Mukasa and Dalziel, 2000) and in the Ellsworth-Whitmore Mountains (~170–210 Ma K-Ar whole rock and U-Pb zircon; Craddock et al., 2017). Older Triassic magmatic intrusions (~200–250 Ma; obtained by various dating methods) are well recorded on Thurston Island (Pankhurst et al., 1993), along the Walgreen Coast (Kipf et al., 2012; Mukasa and Dalziel, 2000), and as inherited U-Pb zircon ages in the Jurassic intrusions of the Ellsworth-Whitmore Mountains (Craddock et al., 2017). Notably, the lack of 100–115 Ma old mineral grains in eastern Pine Island Bay sediments argues for the absence of a mid-Cetaceous orogenic belt below the PIG drainage basin. This observation could be explained by complete erosion of Cretaceous rocks by PIG and subsequent erosion of deeper and older basement batholiths. Alternatively, the granitic basement underlying PIG could have been emplaced in a back-arc setting during the mid-Cretaceous flare-up event (Pankhurst et al., 1993; Zundel et al., 2019).

An interesting feature in the thermochronological ages presented is the ~35 Ma $^{40}Ar/^{39}Ar$ age peak from western Pine Island Bay. We suggest that this minor feature may be related to a gabbroic intrusive complex below TG. Such rocks only crop out in a single nunatak at Mt. Murphy (Rocchi et al., 2006) However, aeromagnetic investigations confirm the presence of a strong anomaly in the TG drainage basin (Bingham et al., 2012; Golynsky et al., 2018) resembling magnetic anomalies related to outcrops of mafic gabbro-tonalite-granodiorite suites in other sectors of Antarctica (Vaughan et al., 1998). Support for this interpretation comes from our PCA map (Fig. 6), where western Pine Island Bay is characterised by positive PC1 loading of several elements, which are indicative of mafic sources (i.e. Fe_2O_3, V, Ni, Co, Cr and Sc). Thwaites Glacier is hence likely to be a major supplier of mafic minerals, such as pyroxene and olivine (and maybe also hornblende and biotite) to the offshore. Supply of mafic minerals, such as magnetite, goethite and hematite, to Pine Island Bay originates mainly from TG, as evidenced by the pronounced magnetic signature (i.e. IRM_{100mT} and HIRM) of ice-proximal sediments (Fig. 6 and Appendix Table 1). While magnetite is indicative of the presence of mafic rocks below the TG catchment, hematite and goethite are more likely to originate from sedimentary rocks (Liu et al., 2012) and, therefore, their supply into Pine Island Bay points to erosion of the (pre-Oligocene) kaolinite-bearing sedimentary strata below the TG catchment (Ehrmann et al., 2011).

6.3. Relationship between different provenance tracers

Overall, we observe that the various geochemical, mineralogical and magnetic signatures of seafloor surface sediments in Pine Island Bay follow a consistent geographic trend from east to west, i.e. from PIG to TG (Fig. 3; Appendix Fig. 1). For instance, the Sr and Nd isotope fingerprint of the <63 μm-fraction generally co-varies with the clay mineralogical signature of the <2 μm-fraction, with detritus supplied by PIG being initially mixed with detritus supplied by the Northern Ice Shelf, and subsequently by detritus delivered by TG. A minor component of detritus might be delivered from glaciers feeding into the Crosson Ice Shelf to westernmost Pine Island Bay, as it is suggested by the slightly higher ε_{Nd} values of sediments at sites 22 and 23, which are located in the vicinity of a minor bathymetric trough extending NNE-wards from the westernmost Crosson Ice Shelf (i.e., their ε_{Nd} data trend towards the ε_{Nd} signature of sediments at site PS69/281 located at the east coast of Bear Island) (Fig. 1, lower panel).

Similarly, the provenance signals of $^{40}Ar/^{39}Ar$ ages of iceberg-rafted hornblende and biotite grains and fine grained (ε_{Nd}, smectite/illite) glacigenic detritus in the sediments from eastern, central and western Pine Island Bay are generally coupled (Fig. 5). When grouping the IRD age populations into different classes, we observe that the peaks spanning 110–170 Ma and > 270 Ma become more pronounced from eastern to western Pine Island Bay, while the peak spanning 170–270 Ma becomes less pronounced. This trend correlates with an increase of smectite/illite ratios and ε_{Nd} values from east to west and indicates a similar sediment delivery route for the fine-grained and iceberg-rafted detritus within Pine Island Bay.

Mixing of detritus supplied by PIG and TG occurs mainly in central and western Pine Island Bay, explaining the shifts in $^{40}Ar/^{39}Ar$ age population and fine-grained provenance signatures. The observed similar distribution patterns between the various provenance proxies for different particle sizes indicate absence of large-scale grain-size or mineral sorting during sediment transport in Pine Island Bay. Glacigenic sediment is deposited in the bay through melt-out of IRD from icebergs calved at the nearby coast or meltwater plumes generated by ocean-induced melting at the ice shelf base and the grounding line. Iceberg-rafting usually delivers unsorted glacigenic debris of various grain sizes, while meltwater can only supply fine-grained particles (e.g., Diekmann and Kuhn, 1999). Hence, our data may suggest iceberg-rafting as the dominant sediment transport mechanism in Pine Island Bay.

However, strong geological evidence for modern plumite deposition in the bay indicates that today meltwater is a major supplier of glacigenic detritus (e.g., Witus et al., 2014; Smith et al., 2017). If we consider the distribution of glacial meltwater concentrations in Pine Island Bay as a proxy for the distribution of suspended particle load, all our studied sites must be located in the shelf region that is mostly affected by plumite deposition (e.g. Nakayama et al., 2013; Biddle et al., 2019). Furthermore, we can conclude at least for eastern Pine Island Bay that meltwater-derived sedimentation there must indeed mainly originate from PIG due to the existence of a cyclonic gyre immediately seaward of the PIG Ice Shelf front (e.g., Naveira Garabato et al., 2017), which probably focusses deposition of PIG-derived plumites proximal to this glacier.

Samples from more distal mid-shelf sites in the eastern Amundsen Sea Embayment (i.e. site BC485 and PS69/299; Simões Pereira et al., 2018; for locations, see Fig. 1) indicate a more complex admixture of detritus with increasing distance from PIG and TG (Figs. 4, 5). At present, the IRD provenance signals sourced from PIG and TG cannot be traced over long distances across the Amundsen Sea Embayment shelf, indicating that the signals are either not carried very far, or that they become overprinted by IRD input from other sources with increasing distance from the ice-shelf fronts. An important factor may be that in the Amundsen Sea Embayment only PIG and TG are capable of calving icebergs with sizes exceeding several hundred square kilometres (e.g., Stammerjohn et al., 2015; Arndt et al., 2018). Because the residence time of an iceberg increases considerably with its size (Mazur et al., 2019), especially when a huge, deep-keeled icebergs calved from PIG or TG runs aground, this increases the potential for ocean-induced melt-out of sub- and englacial debris in close proximity to the source glacier. In general, however, large tabular icebergs calved from Antarctic ice shelves are believed to carry only minor quantities of IRD because most of the basal debris melts out at the grounding line, where the base of the ice is in contact with relatively warm ocean water (e.g. Anderson, 1999;

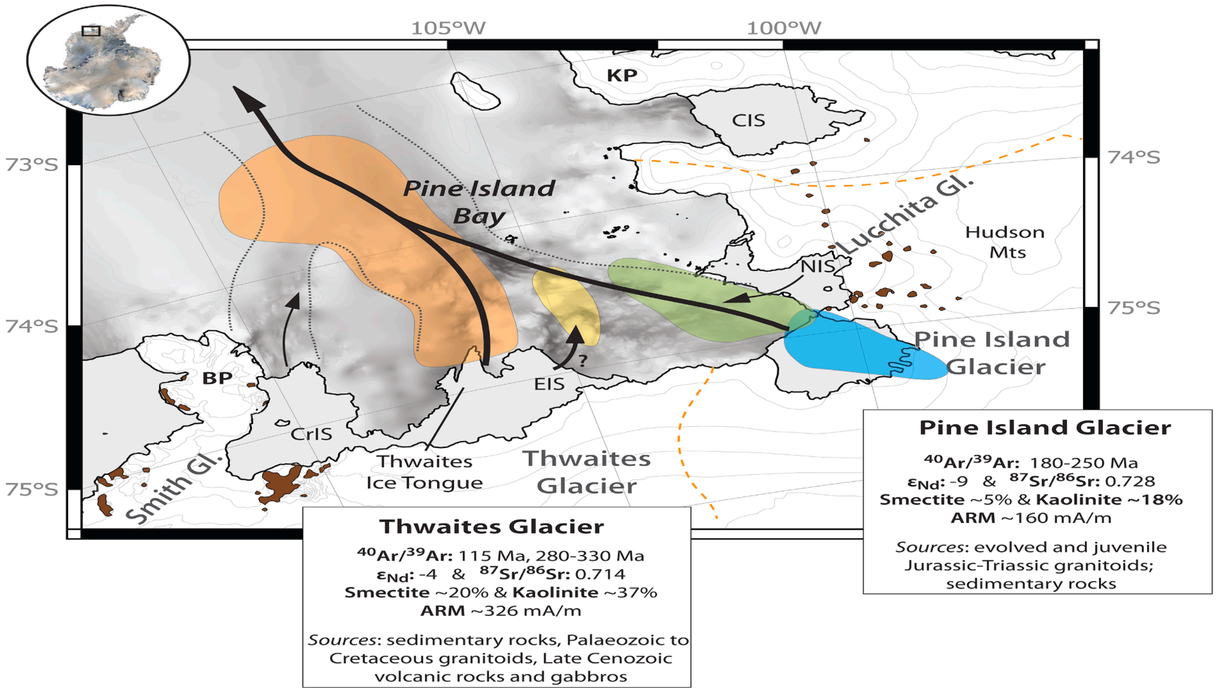

Fig. 7. Summary figure of major transport pathways of glacigenic detritus in Pine Island Bay. Coloured fields denote geographical sectors as discussed in the text and are based on the fields displayed in Fig. 6. Text boxes summarize notable geochemical, clay mineralogical and rock magnetic properties used to discern the provenance fingerprints of Pine Island Glacier and Thwaites Glacier. Suggested rock sources below the two major ice streams are also reported. Dashed grey lines denote the Pine Island-Thwaites paleo-ice stream trough, as well as an unnamed trough further west. BP: Bear Peninsula, CIS: Cosgrove Ice Shelf, CrIS: Crosson Ice Shelf, EIS: Eastern Ice Shelf, KP: King Peninsula, NIS: Northern Ice Shelf. (For interpretation of the references to colour in this figure legend, the reader is referred to the web version of this article).

Williams et al., 2010). We therefore suggest that today the eastern Amundsen Sea coast (including Thurston Island) is a more important source for the offshore supply of IRD than the ice margins along the southern coast of Pine Island Bay, including PIG and TG. The eastern Amundsen Sea coast is topographically more elevated and has more outcrops than the downstream sections of PIG and TG (Burton-Johnson et al., 2016), implying that glaciers draining this area are likely to carry more englacial and supraglacial detritus. Thus, icebergs that eventually calve from this coast should be debris-laden. These icebergs first travel south across the shelf before turning westwards (Mazur et al., 2019), and thus may explain the 100 Ma age peak in the IRD from the central Pine Island Bay samples (Fig. 4).

7. Concluding geochemical characterization of glacigenic detritus sourced from Pine Island and Thwaites glaciers

The provenance signature of detritus supplied by PIG and TG can be assigned with a high degree of confidence due to the analysis of (sub-ice) shelf sediments recovered in close proximity to the grounding line. Radiogenic isotope fingerprints and clay-mineral assemblages of fine-grained detritus and thermochronological data from coarse-grained iceberg-rafted grains in particular provide detailed knowledge on the provenance signatures of glacigenic detritus sourced from these major ice streams as well as the sub-ice geology below the different ice drainage catchments. Our results indicate that the subglacial bed in the PIG drainage basin is composed of evolved Jurassic granites and/or Jurassic to Early Palaeozoic granitoids, and probably sedimentary strata originating from erosion of these bedrock sources. The most striking characteristic of the thermochronological dates of the igneous bedrock in the PIG catchment is the prevalence of 170 to 270 Ma ages signalling absence of Cretaceous intrusives, which are widespread across West Antarctica (Simões Pereira et al., 2018). Subglacial erosion of the lithologies underneath PIG produces fine-grained glacigenic detritus characterised by low ε_{Nd} values (~ -9), high $^{87}Sr/^{86}Sr$ ratios (~0.728), and relatively low smectite (~5%) and kaolinite contents (~18%) (Fig. 7).

The provenance fingerprint of detritus supplied by TG is distinct from that delivered by PIG. One of the most striking observations of this study is that TG supplies detritus with notably higher ε_{Nd} values (~ -4) and lower $^{87}Sr/^{86}Sr$ ratios (0.714) than the detritus supplied by PIG. The substrate underlying the TG system is a major source of kaolinite ($\leq$37%), indicating erosion of widespread pre-Oligocene sedimentary strata, as well as smectite ($\leq$20%), supporting the presence of mafic sources in its ice drainage basin. Hornblende and biotite grains are characterised by a broad $^{40}Ar/^{39}Ar$ age spectrum spanning 110 to 380 Ma, with a pronounced age peak at ~115 Ma, as well as a minor age peak at ~35 Ma. Overall, our thermochronological data hints at the erosion of hornblende- and biotite-bearing granitoids (e.g. granites, granodiorites, tonalites) of Cretaceous to Palaeozoic ages, as well as gabbroic rocks of Oligocene age. Our conclusion of the presence of both bedrock and sedimentary substrate in the TG drainage basin is in agreement with the interpretation of airborne radar data (Schroeder et al., 2014b). Crystalline bedrock is assumed to mainly occur in the lower trunk of TG, resembling the inner shelf part of the Pine Island-Thwaites paleo-ice stream trough (e.g. Lowe and Anderson, 2003; Nitsche et al., 2013). In addition, high aeromagnetic anomalies (Bingham et al., 2012; Golynsky et al., 2018) and high geothermal fluxes (Schroeder et al., 2014a) below the central portion of TG are consistent with the presence of mafic rocks (volcanic, gabbro) at its bed.

Our study provides a new perspective on the subglacial geology below the WAIS, which is not only important for a better understanding of the geological evolution of West Antarctica, but also provides the tools for reconstructing paleo-ice sheet configurations on the continent based on geochemical and mineralogical provenance analyses of marine sediments.

Declaration of competing interest

The authors declare that they have no known competing financial interests or personal relationships that could have appeared to influence the work reported in this paper.

Acknowledgments

P.S.P. thanks the Kristian Gerhard Jebsen Foundation for a PhD scholarship, Katharina Kreissig and Barry Coles for technical assistance in the lab and Pieter Vermeesch for constructive discussion on the statistical methodology. Werner Ehrmann and the Institute of Geophysics and Geology, University of Leipzig, is warmly thanked for their help and support with the clay mineral analyses. U.S. National Science Foundation grant 0348274 is acknowledged by S. Brachfeld and C. Doherty, and U.K. Natural Environment Research Council (NERC) Grant NE/M013081/1 is acknowledged by J.A. Smith and C.-D. Hillenbrand. NERC UK IODP is acknowledged for providing funding to P.S.P. and T.v.d.F. to participate in the PS104 expedition to the Amundsen Sea. We also thank the shipboard scientific parties, captains, officers and crews of the various expeditions and are grateful to the three anonymous reviewers, whose thoughtful comments improved this paper.

Appendix A. Supplementary data

Supplementary data to this article can be found online at https://doi.org/10.1016/j.chemgeo.2020.119649.

References

Anderson, J.B., 1999. Antarctic Marine Geology. Cambridge University Press.

Arndt, J.E., Schenke, H.W., Jakobsson, M., Nitsche, F.O., Buys, G., Goleby, B., Rebesco, M., Bohoyo, F., Hong, J., Black, J., Greku, R., Udintsev, G., Barrios, F., Reynoso-Peralta, W., Taisei, M., Wigley, R., 2013. The International Bathymetric Chart of the Southern Ocean (IBCSO) version 1.0-a new bathymetric compilation covering circum-Antarctic waters. Geophys. Res. Lett. 40, 3111–3117. https://doi.org/10.1002/grl.50413.

Arndt, J.E., Larter, R.D., Friedl, P., Gohl, K., Höppner, K., the Science Team of Expedition PS104, 2018. Bathymetric controls on calving processes at Pine Island Glacier. Cryosphere 12, 2039–2050.

Banerjee, S.K., King, J., Marvin, J., 1981. A rapid method for magnetic granulometry with applications to environmental studies. Geophys. Res. Lett. 8 (4), 333–336.

Bayon, G., German, C.R., Boella, R.M., Milton, J.A., Taylor, R.N., Nesbitt, R.W., 2002. An improved method for extracting marine sediment fractions and its application to Sr and Nd isotopic analysis. Chem. Geol. 187 (3–4), 179–199.

Behrendt, J.C., 2013. The aeromagnetic method as a tool to identify Cenozoic magmatism in the West Antarctic Rift System beneath the West Antarctic Ice Sheet - a review; Thiel subglacial volcano as possible source of the ash layer in the WAISCORE. Tectonophysics 585, 124–136. https://doi.org/10.1016/j.tecto.2012.06.035.

Biddle, L.C., Loose, B., Heywood, K.J., 2019. Upper ocean distribution of glacial meltwater in the Amundsen Sea, Antarctica. J. Geophys. Res. 124, 6,854–6,870. https://doi.org/10.1029/2019JC015133.

Bingham, R.G., Ferraccioli, F., King, E.C., Larter, R.D., Pritchard, H.D., Smith, A.M., Vaughan, D.G., 2012. Inland thinning of West Antarctic Ice Sheet steered along subglacial rifts. Nature 487, 468–471. https://doi.org/10.1038/nature11292.

Biscaye, P.E., 1964. Distinction between kaolinite and chlorite in recent sediments by X-ray diffraction. Am. Mineral. 49, 1281–1289.

Biscaye, P.E., 1965. Mineralogy and sedimentation of recent deep-sea clay in the Atlantic Ocean and adjacent seas and oceans. Geol. Soc. Am. Bull. 76 (7), 803–832.

Bloemendal, J., King, J.W., Hall, F.R., Doh, S.J., 1992. Rock magnetism of Late Neogene and Pleistocene deep-sea sediments: relationship to sediment source, diagenetic processes, and sediment lithology. J. Geophys. Res. 97 (B4), 4361–4375.

Boulton, G.S., 1996. Theory of glacial erosion, transport and deposition as a consequence of subglacial sediment deformation. J. Glaciol. 42, 43–62. https://doi.org/10.3189/S0022143000030525.

Burton-Johnson, A., Black, M., Fretwell, P.T., Kaluza-Gilbert, J., 2016. An automated methodology for differentiating rock from snow, clouds and sea in Antarctica from Landsat 8 imagery: a new rock outcrop map and area estimation for the entire Antarctic continent. Cryosphere 10, 1665–1677. https://doi.org/10.5194/tc-10-1665-2016.

Chester, R., Hughes, M.J., 1967. A chemical technique for the separation of ferro-manganese minerals, carbonate minerals and adsorbed trace elements from pelagic sediments. Chem. Geol. 2, 249–262.

Collier, R., Edmond, J., 1984. The trace element geochemistry of marine biogenic particulate matter. Prog. Oceanogr. 13 (2), 113–199.

Cook, C.P., Van De Flierdt, T., Williams, T., Hemming, S.R., Iwai, M., Kobayashi, M., Jimenez-Espejo, F.J., Escutia, C., González, J.J., Khim, B.K., McKay, R.M., Passchier, S., Bohaty, S.M., Riesselman, C.R., Tauxe, L., Sugisaki, S., Galindo, A.L., Patterson, M.O., Sangiorgi, F., Pierce, E.L., Brinkhuis, H., Klaus, A., Fehr, A., Bendle, J.A.P., Bijl, P.K., Carr, S.A., Dunbar, R.B., Flores, J.A., Hayden, T.G., Katsuki, K., Kong, G.S., Nakai, M., Olney, M.P., Pekar, S.F., Pross, J., Röhl, U., Sakai, T., Shrivastava, P.K., Stickley, C.E., Tuo, S., Welsh, K., Yamane, M., 2013. Dynamic behaviour of the East Antarctic ice sheet during Pliocene warmth. NatureGeosci 6, 765–769. https://doi.org/10.1038/ngeo1889.

Craddock, J.P., Fitzgerald, P., Konstantinou, A., Nereson, A., Thomas, R.J., 2017. Detrital zircon provenance of upper Cambrian-Permian strata and tectonic evolution of the Ellsworth Mountains, West Antarctica. Gondwana Res. 45, 191–207. https://doi.org/10.1016/J.GR.2016.11.011.

Dalrymple, G.B., Alexander Jr., E.C., Lanphere, M.A., Kraker, G.P., 1981. Irradiation of samples for 40Ar/39Ar dating using the Geological Survey TRIGA reactor. U.S. Geological Survey Professional Paper 1176.

DeConto, R.M., Pollard, D., 2016. Contribution of Antarctica to past and future sea-level rise. Nature 531, 591–597. https://doi.org/10.1038/nature17145.

Diekmann, B., Kuhn, G., 1999. Provenance and dispersal of glacial–marine surface sediments in the Weddell Sea and adjoining areas, Antarctica: ice-rafting versus current transport. Mar. Geol. 158, 209–231. https://doi.org/10.1016/S0025-3227(98)00165-0.

Dutton, A., Carlson, A.E., Long, A.J., Milne, G.A., Clark, P.U., DeConto, R., Horton, B.P., Rahmstorf, S., Raymo, M.E., 2015. Sea-level rise due to polar ice-sheet mass loss during past warm periods. Science 349. https://doi.org/10.1126/science.aaa4019.

Ehrmann, W.U., Melles, M., Kuhn, G., Grobe, H., 1992. Significance of clay mineral assemblages in the Antarctic Ocean. Mar. Geol. 107, 249–273. https://doi.org/10.1016/0025-3227(92)90075-S.

Ehrmann, W., Hillenbrand, C.-D., Smith, J.A., Graham, A.G.C., Kuhn, G., Larter, R.D., 2011. Provenance changes between recent and glacial-time sediments in the Amundsen Sea embayment, West Antarctica: clay mineral assemblage evidence. Antarct. Sci. 23, 471–486. https://doi.org/10.1017/S0954102011000320.

Frederichs, T., Bleil, U., Däumler, K., von Dobeneck, T., Schmidt, A., 1999. The magnetic view on the marine paleoenvironment: parameters, techniques and potentials of rock magnetic studies as a key to paleoclimatic and paleoceanographic changes. In: Fischer, G., Wefer, G. (Eds.), Use of Proxies in Paleoceanography: Examples From the South Atlantic. Springer, Berlin Heidelberg, pp. 575–599.

Fretwell, P., Pritchard, H.D., Vaughan, D.G., Bamber, J.L., Barrand, N.E., Bell, R., Bianchi, C., Bingham, R.G., Blankenship, D.D., Casassa, G., Catania, G., Callens, D., Conway, H., Cook, A.J., Corr, H.F.J., Damaske, D., Damm, V., Ferraccioli, F., Forsberg, R., Fujita, S., Gim, Y., Gogineni, P., Griggs, J.A., Hindmarsh, R.C.A., Holmlund, P., Holt, J.W., Jacobel, R.W., Jenkins, A., Jokat, W., Jordan, T., King, E.C., Kohler, J., Krabill, W., Riger-Kusk, M., Langley, K.A., Leitchenkov, G., Leuschen, C., Luyendyk, B.P., Matsuoka, K., Mouginot, J., Nitsche, F.O., Nogi, Y., Nost, O.A., Popov, S.V., Rignot, E., Rippin, D.M., Rivera, A., Roberts, J., Ross, N., Siegert, M.J., Smith, A.M., Steinhage, D., Studinger, M., Sun, B., Tinto, B.K., Welch, B.C., Wilson, D., Young, D.A., Xiangbin, C., Zirizzotti, A., 2013. Bedmap2: improved ice bed, surface and thickness datasets for Antarctica. Cryosphere 7, 375–393. https://doi.org/10.5194/tc-7-375-2013.

Futa, K., Le Masurier, W.E., 1983. Nd and Sr isotopic studies on cenozoic mafic lavas from West Antarctica: another source for continental alkali basalts. Contrib. Mineral. Petrol. 83, 38–44. https://doi.org/10.1007/BF00373077.

Golynsky, A.V., Ferraccioli, F., Hong, J.K., Golynsky, D.A., von Frese, R.R.B., Young, D.A., Blankenship, D.D., Holt, J.W., Ivanov, S.V., Kiselev, A.V., Masolov, V.N., Eagles, G., Gohl, K., Jokat, W., Damaske, D., Finn, C., Aitken, A., Bell, R.E., Armadillo, E., Jordan, T.A., Greenbaum, J.S., Bozzo, E., Caneva, G., Forsberg, R., Ghidella, M., Galindo-Zaldivar, J., Bohoyo, F., Martos, Y.M., Nogi, Y., Quartini, E., Kim, H.R., Roberts, J.L., 2018. New magnetic anomaly map of the Antarctic. Geophys. Res. Lett. 45, 6437–6449. https://doi.org/10.1029/2018GL078153.

Graham, A.G.C., Larter, R.D., Gohl, K., Dowdeswell, J.A., Hillenbrand, C.-D., Smith, J.A., Evans, J., Kuhn, G., Deen, T., 2010. Flow and retreat of the Late Quaternary Pine Island-Thwaites palaeo-ice stream, West Antarctica. J. Geophys. Res. 115, 3025. https://doi.org/10.1029/2009JF001482.

Grousset, F.E., Parra, M., Bory, A., Martinez, P., Bertrand, P., Shimmield, G., Ellam, R.M., 1998. Saharan wind regimes traced by the Sr–Nd isotopic composition of subtropical Atlantic sediments: last glacial maximum vs today. Quat. Sci. Rev. 17 (4–5), 395–409.

Hillenbrand, C.-D., Ehrmann, W., 2002. Distribution of clay minerals in drift sediments on the continental rise west of the Antarctic Peninsula, ODP Leg 178, Sites 1095 and 1096. In: Barker, P.F., Camerlenghi, A., Acton, G.D., Ramsay, A.T.S. (Eds.), Proc. ODP Sci. Results 178. Ocean Drilling Program, Texas A&M University, College Station, TX 77845–9547, U.S.A, pp. 1–29 (CD-ROM). Available from.

Hillenbrand, C.-D., Fütterer, D.K., Grobe, H., Frederichs, T., 2002. No evidence for a Pleistocene collapse of the West Antarctic Ice Sheet from continental margin sediments recovered in the Amundsen Sea. Geo-Marine Lett 22, 51–59. https://doi.org/10.1007/s00367-002-0097-7.

Hillenbrand, C.-D., Grobe, H., Diekmann, B., Kuhn, G., Fütterer, D.K., 2003. Distribution of clay minerals and proxies for productivity in surface sediments of the Bellingshausen and Amundsen seas (West Antarctica) - relation to modern environmental conditions. Mar. Geol. 193, 253–271. https://doi.org/10.1016/S0025-3227(02)00659-X.

Hillenbrand, C.-D., Kuhn, G., Frederichs, T., 2009. Record of a Mid-Pleistocene depositional anomaly in West Antarctic continental margin sediments: an indicator for ice-sheet collapse? Quat. Sci. Rev. 28, 1147–1159. https://doi.org/10.1016/j.quascirev.2008.12.010.

Hillenbrand, C.-D., Kuhn, G., Smith, J.A., Gohl, K., Graham, A.G.C., Larter, R.D., Klages, J.P., Downey, R., Moreton, S.G., Forwick, M., Vaughan, D.G., 2013. Grounding-line retreat of the West Antarctic Ice Sheet from inner Pine Island Bay. Geology 41, 35–38. https://doi.org/10.1130/G33469.1.

Hillenbrand, C.-D., Smith, J.A., Hodell, D.A., Greaves, M., Poole, C.R., Kender, S., Williams, M., Andersen, T.J., Jernas, P.E., Elderfield, H., Klages, J.P., Roberts, S.J., Gohl, K., Larter, R.D., Kuhn, G., 2017. West Antarctic Ice Sheet retreat driven by Holocene warm water intrusions. Nature 547, 43–48.

Holt, J.W., Blankenship, D.D., Morse, D.L., Young, D.A., Peters, M.E., Kempf, S.D., Richter, T.G., Vaughan, D.G., Corr, H.F.J., 2006. New boundary conditions for the West Antarctic Ice Sheet: subglacial topography of the Thwaites and Smith glacier catchments. Geophys. Res. Lett. 33, 2–5. https://doi.org/10.1029/2005GL025561.

Hughes, T.J., 1981. The weak underbelly of the West Antarctic Ice- Sheet. J. Glaciol. 25, 5–57.

Jacobs, S.S., Jenkins, A., Giulivi, C.F., Dutrieux, P., 2011. Stronger ocean circulation and increased melting under Pine Island Glacier ice shelf. Nat. Geosci. 4, 519–523. https://doi.org/10.1038/ngeo1188.

Jakobsson, M., Anderson, J.B., Nitsche, F.O., Gyllencreutz, R., Kirshner, A.E., Kirchner, N., O'Regan, M., Mohammad, R., Eriksson, B., 2012. Ice sheet retreat dynamics inferred from glacial morphology of the central Pine Island Bay Trough, West Antarctica. Quat. Sci. Rev. 38, 1–10. https://doi.org/10.1016/j.quascirev.2011.12.017.

Jenkins, A., Shoosmith, D., Dutrieux, P., Jacobs, S., Kim, T.W., Lee, S.H., Ha, H.K., Stammerjohn, S., 2018. West Antarctic Ice Sheet retreat in the Amundsen Sea driven by decadal oceanic variability. Nat. Geosci. https://doi.org/10.1038/s41561-018-0207-4.

Jeong, S., Howat, I.M., Bassis, J.N., 2016. Accelerated ice shelf rifting and retreat at Pine Island Glacier, West Antarctica. Geophys. Res. Lett. https://doi.org/10.1002/2016GL071360.

Johnson, J.S., Bentley, M.J., Smith, J.A., Finkel, R.C., Rood, D.H., Gohl, K., Balco, G., Larter, R.D., Schaefer, J.M., 2014. Rapid thinning of Pine Island Glacier in the early Holocene. Science 343, 999–1001. https://doi.org/10.1126/science.1247385.

Jordan, T.A., Ferraccioli, F., Vaughan, D.G., Holt, J.W., Corr, H., Blankenship, D.D., Diehl, T.M., 2010. Aerogravity evidence for major crustal thinning under the Pine Island Glacier region (West Antarctica). Geol. Soc. Am. Bull. 122, 714–726. https://doi.org/10.1130/B26417.1.

Joughin, I., Tulaczyk, S., Bamber, J.L., Blankenship, D., Holt, J.W., Scambos, T., Vaughan, D.G., 2009. Basal conditions for Pine Island and Thwaites Glaciers, West Antarctica, determined using satellite and airborne data. J. Glaciol. 55, 245–257. https://doi.org/10.3189/002214309788608705.

Joughin, I., Smith, B.E., Medley, B., 2014. Marine ice sheet collapse potentially under way for the thwaites glacier basin, West Antarctica. Science 344, 735–738. https://doi.org/10.1126/science.1249055.

Kellogg, T.B., Kellogg, D.E., 1987. Recent glacial history and rapid ice stream retreat in the Amundsen Sea. J. Geophys. Res. 92 (B9), 8859–8864.

King, J.W., Banerjee, S.K., Marvin, J., Özdemir, Ö., 1982. A comparison of different magnetic methods for determining the relative grain size of magnetite in natural materials: some results from lake sediments. Earth Planet. Sci. Lett. 59, 404–419.

Kingslake, J., Scherer, R.P., Albrecht, T., Coenen, J., Powell, R.D., Reese, R., Stansell, N.D., Tulaczyk, S., Wearing, M.G., Whitehouse, P.L., 2018. Extensive retreat and re-advance of the West Antarctic Ice Sheet during the Holocene. Nature. https://doi.org/10.1038/s41586-018-0208-x.

Kipf, A., Mortimer, N., Werner, R., Gohl, K., Van Den Bogaard, P., Hauff, F., Hoernle, K., 2012. Granitoids and dykes of the Pine Island Bay region, West Antarctica. Antarct. Sci. 24, 473–484. https://doi.org/10.1017/S0954102012000259.

Kirshner, A.E., Anderson, J.B., Jakobsson, M., O'Regan, M., Majewski, W., Nitsche, F.O., 2012. Post-LGM deglaciation in Pine Island Bay, West Antarctica. Quat. Sci. Rev. 38, 11–26. https://doi.org/10.1016/j.quascirev.2012.01.017.

Klages, J.P., Kuhn, G., Hillenbrand, C.-D., Graham, A.G.C., Smith, J.A., Larter, R.D., Gohl, K., 2013. First geomorphological record and glacial history of an inter-ice stream ridge on the West Antarctic continental shelf. Quat. Sci. Rev. 61, 47–61.

Klages, J.P., Kuhn, G., Hillenbrand, C.-D., Smith, J.A., Graham, A.G., Nitsche, F.O., Jernas, P.E., Gohl, K., Wacker, L., 2017. Limited grounding-line advance onto the West Antarctic continental shelf in the easternmost Amundsen Sea Embayment during the last glacial period. PLoS One 12 (7), e0181593. https://doi.org/10.1371/journal.pone.0181593.

Kuiper, K.F., Deino, A., Hilgen, F.J., Krijgsman, W., Renne, P.R., Wijbrans, J.R., 2008. Synchronizing rock clocks of Earth history. Science 320 (5875), 500–504.

Larter, R.D., Anderson, J.B., Graham, A.G.C., Gohl, K., Hillenbrand, C.-D., Jakobsson, M., Johnson, J.S., Kuhn, G., Nitsche, F.O., Smith, J.A., Witus, A.W., Bentley, M.J., Dowdeswell, J.A., Ehrmann, W., Klages, J.P., Lindow, J., Ó Cofaigh, C., Spiegel, C., 2014. Reconstruction of changes in the Amundsen Sea and Bellingshausen Sea sector of the West Antarctic Ice Sheet since the Last Glacial Maximum. Quat. Sci. Rev. 100, 55–86.

Lee, J.-Y., Marti, K., Severinghaus, J.P., Kawamura, K., Yoo, H.-S., Lee, J.B., Kim, J.S., 2006. A redetermination of the isotopic abundances of atmospheric Ar. Geochim. Cosmochim. Acta 70 (17), 4507–4512.

LeMasurier, W., 2013. Shield volcanoes of Marie Byrd Land, West Antarctic rift: oceanic island similarities, continental signature, and tectonic controls. Bull. Volcanol. 75, 1–18. https://doi.org/10.1007/s00445-013-0726-1.

Licht, K.J., Hemming, S.R., 2017. Analysis of Antarctic glacigenic sediment provenance through geochemical and petrologic applications. Quat. Sci. Rev. 164, 1–24. https://doi.org/10.1016/j.quascirev.2017.03.009.

Liu, Q., Roberts, A.P., Larrasoaa, J.C., Banerjee, S.K., Guyodo, Y., Tauxe, L., Oldfield, F., 2012. Environmental magnetism: principles and applications. Rev. Geophys. 50, 1–50. https://doi.org/10.1029/2012RG000393.

Liu, Y., Moore, J.C., Cheng, X., Gladstone, R.M., Bassis, J.N., Liu, H., Wen, J., Hui, F., 2015. Ocean-driven thinning enhances iceberg calving and retreat of Antarctic ice shelves. Proc. Natl. Acad. Sci. U. S. A. 112, 3263–3268. https://doi.org/10.1073/pnas.1415137112.

Lowe, A.L., Anderson, J.B., 2003. Evidence for abundant subglacial meltwater beneath the paleo-ice sheet in Pine Island Bay, Antarctica. J. Glaciol. 49, 125–138. https://doi.org/10.3189/172756503781830971.

Ludwig, K.R., 2003. Isoplot 3.00: A Geochronological Toolkit for Microsoft Excel. Berkeley Geochronology Center, Berkeley, CA.

Mazur, A.K., Wåhlin, A.K., Krężel, A., 2017. An object-based SAR image iceberg detection algorithm applied to the Amundsen Sea. Remote Sens. Environ. 189, 67–83. https://doi.org/10.1016/j.rse.2016.11.013.

Mazur, A.K., Wåhlin, A., Kalén, O., 2019. The life cycle of small- to medium-sized icebergs in the Amundsen Sea Embayment. Polar Res. 38, 3313. https://doi.org/10.33265/polar.v38.3313.

Mouginot, J., Rignot, E., Schleuchl, B., 2014. Stronger ocean circulation and increased melting under Pine Island Glacier ice shelf. Geophys. Res. Lett. 41, 1576–1584. https://doi.org/10.1002/2013GL059069.

Mukasa, S.B., Dalziel, I.W.D., 2000. Marie Byrd Land, West Antarctica: evolution of Gondwana's Pacific margin constrained by zircon U-Pb geochronology and feldspar common-Pb isotopic compositions. Geol. Soc. Am. Bull. 112, 611–627. https://doi.org/10.1130/0016-7606.

Muto, A., Peters, L.E., Gohl, K., Sasgen, I., Alley, R.B., Anandakrishnan, S., Riverman, K.L., 2016. Subglacial bathymetry and sediment distribution beneath Pine Island Glacier ice shelf modeled using aerogravity and in situ geophysical data: new results. Earth Planet. Sci. Lett. 433, 63–75. https://doi.org/10.1016/J.EPSL.2015.10.037.

Nakayama, Y., Schröder, M., Hellmer, H., 2013. From circumpolar deep water to the glacial meltwater plume on the eastern Amundsen Shelf. Deep-Sea Res. I 77, 50–62. https://doi.org/10.1016/j.dsr.2013.04.001.

Naveira Garabato, A.C., Forryan, A., Dutrieux, P., Brannigan, L., Biddle, L.C., Heywood, K.J., Jenkins, A., Firing, Y.L., Kimura, S., 2017. Vigorous lateral export of the meltwater outflow from beneath an Antarctic ice shelf. Nature 542, 219–222. https://doi.org/10.1038/nature20825.

Nitsche, F.O., Jacobs, S.S., Larter, R.D., Gohl, K., 2007. Bathymetry of the Amundsen Sea continental shelf: implications for geology, oceanography, and glaciology. Geochem. Geophys. Geosyst. 8, Q10009. https://doi.org/10.1029/2007GC001694.

Nitsche, F.O., Gohl, K., Larter, R.D., Hillenbrand, C.-D., Kuhn, G., Smith, J.A., Jacobs, S., Anderson, J.B., Jakobsson, M., 2013. Paleo ice flow and subglacial meltwater dynamics in Pine Island Bay, West Antarctica. Cryosphere 7, 249–262. https://doi.org/10.5194/tc-7-249-2013.

Pankhurst, R.J., Millar, I.L., Ginmow, A.M., 1993. The pre-Cenozoic magmatic history of the Thurston Island Crustal Block, West Antarctica. J. Geophys. Res. 98 (B7), 11,835–11,849. https://doi.org/10.1029/93JB01157.

Pankhurst, R.J., Weaver, S.D., Bradshaw, J.D., Storey, B.C., Ireland, T.R., 1998. Geochronology and geochemistry of pre-Jurassic superterranes in Marie Byrd Land, Antarctica. J. Geophys. Res. 103 (B2), 2529–2547.

Paolo, F.S., Fricker, H.A., Padman, L., 2015. Volume loss from Antarctic ice shelves is accelerating. Science 348 (6232), 327–331.

Pe-Piper, G., Triantafyllidis, S., Piper, D.J.W., 2008. Geochemical identification of clastic sediment provenance from known sources of similar geology: the cretaceous Scotian Basin, Canada. J. Sediment. Res. 78, 595–607. https://doi.org/10.2110/jsr.2008.067.

Petschick, R., Kuhn, G., Gingele, F., 1996. Clay mineral distribution in surface sediments of the South Atlantic: sources, transport, and relation to oceanography. Mar. Geol. 130, 203–229. https://doi.org/10.1016/0025-3227(95)00148-4.

Pierce, E.L., Hemming, S.R., Williams, T., van de Flierdt, T., Thomson, S.N., Reiners, P.W., Gehrels, G.E., Brachfeld, S.A., Goldstein, S.L., 2014. A comparison of detrital U-Pb zircon, 40Ar/39Ar hornblende, 40Ar/39Ar biotite ages in marine sediments off East Antarctica: implications for the geology of subglacial terrains and provenance studies. Earth-Sci. Rev. 138, 156–178. https://doi.org/10.1016/j.earscirev.2014.08.010.

Pierce, E.L., van de Flierdt, T., Williams, T., Hemming, S.R., Cook, C.P., Passchier, S., 2017. Evidence for a dynamic East Antarctic ice sheet during the mid-Miocene climate transition. Earth Planet. Sci. Lett. https://doi.org/10.1016/j.epsl.2017.08.011.

Pin, C., Bassin, C., 1992. Evaluation of a strontium-specific extraction chromatographic method for isotopic analysis in geological-materials. Anal. Chim. Acta 269 (2), 249–255.

Pin, C., Zalduegui, J.F.S., 1997. Sequential separation of light rare-earth elements, thorium and uranium by miniaturized extraction chromatography: application to isotopic analyses of silicate rocks. Anal. Chim. Acta 339 (1–2), 79–89.

Pollard, D., DeConto, R.M., 2009. Modelling West Antarctic ice sheet growth and collapse through the past five million years. Nature. https://doi.org/10.1038/nature07809.

Rignot, E., 2002. Rapid bottom melting widespread near Antarctic ice sheet grounding lines. Science 296, 2020–2023. https://doi.org/10.1126/science.1070942.

Rignot, E., Mouginot, J., Morlighem, M., Seroussi, H., Scheuchl, B., 2014. Widespread, rapid grounding line retreat of Pine Island, Thwaites, Smith, and Kohler glaciers, West Antarctica, from 1992 to 2011. Geophys. Res. Lett. 41, 3502–3509. https://doi.org/10.1002/2014GL060140.

Rignot, E., Mouginot, J., Scheuchl, B., van den Broeke, M., van Wessem, M.J., Morlighem, M., 2019. Four decades of Antarctic Ice Sheet mass balance from 1979–2017. Proc.

Natl. Acad. Sci. https://doi.org/10.1073/pnas.1812883116.
Riley, T.R., Flowerdew, M.J., Pankhurst, R.J., Leat, P.T., Millar, I.L., Fanning, C.M., Whitehouse, M.J., 2017. A revised geochronology of Thurston Island, West Antarctica, and correlations along the proto-Pacific margin of Gondwana. Antarct. Sci. 29, 47–60. https://doi.org/10.1017/S0954102016000341.
Riley, T.R., Burton-Johnson, A., Flowerdew, M.J., Whitehouse, M.J., 2018. Episodicity within a mid-Cretaceous magmatic flare-up in West Antarctica: U-Pb ages of the Lassiter Coast intrusive suite, Antarctic Peninsula, and correlations along the Gondwana margin. Geol. Soc. Am. Bull. 1–20. https://doi.org/10.1130/B31800.1.
Rocchi, S., LeMasurier, W.E., Di Vincenzo, G., 2006. Oligocene to Holocene erosion and glacial history in Marie Byrd Land, West Antarctica, inferred from exhumation of the Dorrel Rock intrusive complex and from volcano morphologies. Geol. Soc. Am. Bull. 118, 991–1005. https://doi.org/10.1130/B25675.1.
Rowley, P.D., Laudon, T.S., La Prade, K.E., LeMasurier, W.E., 1990. C.9. Hudson Mountains. In: LeMasurier, W.E., Thomson, J.W. (Eds.), Volcanoes of the Antarctic Plate and Southern Oceans. Antarctic Res. Ser. 48pp. 289–297.
Rutberg, R.L., Hemming, S.R., Goldstein, S.L., 2000. Reduced North Atlantic Deep Water flux to the glacial Southern Ocean inferred from neodymium isotope ratios. Nature 405, 935–938.
Scherer, R.P., Aldahan, A., Tulaczyk, S., Possnert, G., Engelhardt, H., Kamb, B., 1998. Pleistocene collapse of the West Antarctic Ice Sheet. Science 281 (5373), 82–85.
Scheuchl, B., Mouginot, J., Rignot, E., Morlighem, M., Khazendar, A., 2016. Grounding line retreat of Pope, Smith, and Kohler Glaciers, West Antarctica, measured with Sentinel-1a radar interferometry data. Geophys. Res. Lett. https://doi.org/10.1002/2016GL069287.
Schoof, C., 2007. Ice sheet grounding line dynamics: steady states, stability, and hysteresis. J. Geophys. Res. 112, 1–19. https://doi.org/10.1029/2006JF000664.
Schroeder, D.M., Blankenship, D.D., Young, D.A., Quartini, E., 2014a. Evidence for elevated and spatially variable geothermal flux beneath the West Antarctic Ice Sheet. Proc. Natl. Acad. Sci. U. S. A. 111, 9070–9072. https://doi.org/10.1073/pnas.1405184111.
Schroeder, D.M., Blankenship, D.D., Young, D.A., Witus, A.E., Anderson, J.B., 2014b. Airborne radar sounding evidence for deformable sediments and outcropping bedrock beneath Thwaites Glacier, West Antarctica. Geophys. Res. Lett. https://doi.org/10.1002/2014GL061645.
Simões Pereira, P., van de Flierdt, T., Hemming, S.R., Hammond, S.J., Kuhn, G., Brachfeld, S., Doherty, C., Hillenbrand, C.D., 2018. Geochemical fingerprints of glacially eroded bedrock from West Antarctica: detrital thermochronology, radiogenic isotope systematics and trace element geochemistry in Late Holocene glacial-marine sediments. Earth-Science Rev. https://doi.org/10.1016/j.earscirev.2018.04.011.
Smith, A.M., Jordan, T.A., Ferraccioli, F., Bingham, R.G., 2013. Influence of subglacial conditions on ice stream dynamics: seismic and potential field data from Pine Island Glacier, West Antarctica. J. Geophys. Res. 118, 1471–1482. https://doi.org/10.1029/2012JB009582.
Smith, J.A., Hillenbrand, C.D., Kuhn, G., Klages, J.P., Graham, A.G.C., Larter, R.D., Ehrmann, W., Moreton, S.G., Wiers, S., Frederichs, T., 2014. New constraints on the timing of West Antarctic Ice Sheet retreat in the eastern Amundsen Sea since the Last Glacial Maximum. Glob. Planet. Chang. https://doi.org/10.1016/j.gloplacha.2014.07.015.
Smith, J.A., Andersen, T.J., Shortt, M., Gaffney, A.M., Truffer, M., Stanton, T.P., Bindschadler, R., Dutrieux, P., Jenkins, A., Hillenbrand, C.D., Ehrmann, W., Corr, H.F.J., Farley, N., Crowhurst, S., Vaughan, D.G., 2017. Sub-ice-shelf sediments record history of twentieth-century retreat of Pine Island Glacier. Nature 541, 77–80. https://doi.org/10.1038/nature20136.
Stammerjohn, S.E., Maksym, T., Massom, R.A., Lowry, K.E., Arrigo, K.R., Yuan, X., Raphael, M., Randall-Goodwin, E., Sherrell, R.M., Yager, P.L., 2015. Seasonal sea ice changes in the Amundsen Sea, Antarctica, over the period of 1979–2014. Elementa Sci. Anthropocene 3, 55. https://doi.org/10.12952/journal.elementa.000055.
Tanaka, T., Togashi, S., Kamioka, H., Amakawa, H., Kagami, H., Hamamoto, T., Yuhara, M., Orihashi, Y., Yoneda, S., Shimizu, H., Kunimaru, T., Takahashi, K., Yanagi, T., Nakano, T., Fujimaki, H., Shinjo, R., Asahara, Y., Tanimizu, M., Dragusanu, C., 2000. JNdi-1: a neodymium isotopic reference in consistency with LaJolla neodymium. Chem. Geol. 168 (3–4), 279–281.
The IMBIE team, 2018. Mass balance of the Antarctic Ice Sheet from 1992 to 2017. Nature. https://doi.org/10.1038/s41586-018-0179-y.
Vaughan, A.P.M., Wareham, C.D., Johnson, A.C., Kelley, S.P., 1998. A Lower Cretaceous, syn-extensional magmatic source for a linear belt of positive magnetic anomalies: the Pacific Margin Anomaly (PMA), western Palmer Land, Antarctica. Earth Planet. Sci. Lett. 158, 143–155. https://doi.org/10.1016/S0012-821X(98)00054-5.
Vaughan, D.G., Corr, H.F., Ferraccioli, F., Frearson, N., O'Hare, A., Mach, D., Holt, J.W., Blankenship, D.D., Morse, D.L., Young, D.A., 2006. New boundary conditions for the West Antarctic ice sheet: subglacial topography beneath Pine Island Glacier. Geophys. Res. Lett. 33 (9), L09501.
Vermeesch, P., Resentini, A., Garzanti, E., 2016. An R package for statistical provenance analysis. Sediment. Geol. 336, 14–25.
Weis, D., Kieffer, B., Maerschalk, C., Barling, J., De Jong, J., Williams, G.A., Hanano, D., Pretorius, W., Mattielli, N., Scoates, J.S., Goolaerts, A., Friedman, R.M., Mahoney, J.B., 2006. High-precision isotopic characterization of USGS reference materials by TIMS and MC-ICP-MS. Geochem. Geophys. Geosyst. 7. https://doi.org/10.1029/2006GC001283.
Williams, T., van de Flierdt, T., Hemming, S.R., Chung, E., Roy, M., Goldstein, S.L., 2010. Evidence for iceberg armadas from East Antarctica in the Southern Ocean during the late Miocene and early Pliocene. Earth Planet. Sci. Lett. 290, 351–361. https://doi.org/10.1016/j.epsl.2009.12.031.
Witus, A.E., Branecky, C.M., Anderson, J.B., Szczuciński, W., Schroeder, D.M., Blankenship, D.D., Jakobsson, M., 2014. Meltwater intensive glacial retreat in polar environments and investigation of associated sediments: example from Pine Island Bay, West Antarctica. Quat. Sci. Rev. 85, 99–118. https://doi.org/10.1016/j.quascirev.2013.11.021.
van Wyk de Vries, M., Bingham, R.G., Hein, A.S., 2017. A new volcanic province: an inventory of subglacial volcanoes in West Antarctica. Geol. Soc. London, Spec. Publ. SP 461, 7. https://doi.org/10.1144/SP461.7.
Zundel, M., Spiegel, C., Mehling, A., Lisker, F., Hillenbrand, C., Monien, P., Klügel, A., 2019. Thurston Island (West Antarctica) between Gondwana subduction and continental separation: a multistage evolution revealed by apatite thermochronology. Tectonics 38, 878–897. https://doi.org/10.1029/2018TC005150.
Zwally, H.J., Giovinetto, M.B., Beckley, M.A., Saba, J.L., 2012. Antarctic and Greenland drainage systems. GSFC Cryospheric Sciences Laboratory Available at. http://icesat4.gsfc.nasa.gov/cryo_data/ant_grn_drainage_systems.php.